Kinematical Retrievals in Deep Convective Clouds from a Network of Scanning Doppler Radars in Oklahoma during MC3E

Kirk North

Master of Science

Atmospheric and Oceanic Sciences

McGill University

Montreal, Quebec

December 2015

A thesis submitted to McGill University in partial fulfillment of the requirements of the degree of Master of Science

ACKNOWLEDGEMENTS

I would like to take this opportunity to first thank my supervisor and friend Dr. Pavlos Kollias for his wisdom and support throughout my years as a graduate student. Pavlos' advice on topics outside of work and study as well as his sense of humour created a friendly environment that ultimately made life as a graduate student easier. Under his supervision I was able to study and learn a breadth of remote sensing and data analysis topics, expanding my knowledge of Earth's atmosphere and the scientific method. I have a greater appreciation for the clouds and weather that affect our daily lives now that I have been able to study these phenomena through the lens of millimeter and centimeter-wavelength radars.

The research that I have conducted throughout my studies would not have been possible without the U.S. Department of Energy's Atmospheric Radiation Measurement program and its team of scientists and radar engineers. In particular, thank you to Nitin Bharadwaj and Kevin Widener for all their time and effort in maintaining the suite of radars used throughout this thesis.

A special thank you goes out to my colleague and office mate Xiaoli Zhou who was always willing to brainstorm ideas with me for answers to questions that I struggled with. Other McGill colleagues of mine, past and present, deserve recognition as well: Katia Lamer, Paloma Borque, Stefan Kneifel, Ieng Jo, Aleksandra Tatarevic, Jasmine Rémillard, and Arunchandra Chandra. Thank you all for making my time at McGill and abroad more enjoyable and entertaining, and to Katia for translating my abstract into French.

Finally, I would like to express my love and gratitude to my family and friends, in particular my mother and father. Their moral support throughout this process has been immeasurable, especially during the summer of 2012 when I had to undergo open heart surgery for the second time in my life in order to address a congenital heart defect. Much love and admiration to my girlfriend Maggie, who provided words of encouragement throughout the last few years, and who was always understanding of my late nights at the office. I am and will be forever grateful.

CONTRIBUTION OF AUTHORS

The work presented in this thesis was carried out by myself and is based on a manuscript to be submitted to Atmospheric Measurement Techniques, a journal of the European Geosciences Union. This manuscript is co-authored by my supervisor Pavlos Kollias and colleagues Scott Giangrande, Scott Collis, and Corey Potvin, all of whom played normal co-author roles, including standard revision of text and figures.

ABSTRACT

The U.S. Department of Energy's (DOE) Atmospheric Radiation Measurement (ARM) program operates an advanced user facility centralized in the U.S. Southern Great Plains (SGP) near Lamont, Oklahoma. The ARM SGP site includes a heterogeneous scanning Doppler radar network collecting continuous and coordinated Doppler velocity measurements at multiple elevations in deep convective clouds. The surrounding National Weather Service (NWS) Next Generation Weather Surveillance Radar 1988 Doppler (NEXRAD WSR-88D) further supplements this network. Scanning radar measurements are used as input to an optimal estimation three-dimensional variational (3D-VAR) method that retrieves horizontal and vertical air motions over a large analysis domain (100 km x 100 km) at storm-scale resolutions (250 m). Similar methods have been suggested as one possible replacement over traditional multi-Doppler wind retrieval techniques, but they have not been widely implemented and evaluated on real datasets. A practical sensitivity analysis for 3D-VAR wind retrievals is introduced which is capable of finding a range of constraint weights that produce robust wind fields. Following this analysis, it is shown that 3D-VAR vertical air motion retrievals are stable over a large range of constraint weights, with an uncertainty estimate on the order of 1-2 m s^{-1}. A similar sensitivity analysis also indicates that traditional upwards integration techniques do not properly satisfy mass continuity. Evaluation of 3D-VAR vertical velocities with those from collocated 915-MHz radar wind profilers is performed. Mean bias and absolute errors between the two methods are found to

be on the order of 0.5 m s^{-1} and 1 m s^{-1}, respectively, with moderate time-height correlations on the order of 0.5. These results are encouraging and moving forward may lead to better observational datasets used to constrain numerical simulations of convection.

ABRÉGÉ

Le programme Mesure de radiation atmosphérique (ARM) du Département de l'Énergie des États-Unis (DOE) opère plusieurs installations de hautes technologies. La plus grande de ces installations se trouve dans les Grandes plaines du sud près de Lamont en Oklahoma. Elle contient un réseau hétérogène de radar Doppler qui scannent les nuages de convection sévère et qui collecte des informations sur la vitesse Doppler du vent de façon continue et coordonné. Présent aux alentours, le Radar Doppler de surveillance du temps de prochaine génération 1988 (NEXRAD WSR-88D) propriété du Service de météorologie national contribue aussi à cette tâche de façon complémentaire. Les observations des radars de balayage sont utilisées dans un algorithme d'optimisation avec variations en trois dimension (3D-VAR) afin d'estimer les mouvements horizontales et verticales du vent le tout dans un grand domaine (100 km x 100 km) avec une résolution à l'échelle des tempêtes (250 m). Des méthodes similaires ont été suggérées afin de remplacer les méthodes traditionnelles de récupération du vent par multiple Doppler. Toutefois, ces méthodes n'ont pas été ni implémentées ni validées en profondeur avec de vrais ensembles de données. Une analyse de sensibilité pour les récupérations du vent par 3D-VAR est présentée dans cet ouvrage. Cette analyse est pratique et permet de déterminer le poids d'une multitude de contrainte afin de créer résultats robustes. En utilisant cette analyse, il est démontré que les récupération du vent par 3D-VAR sont stables en utilisant une multitude de différent poids avec des estimation d'incertitude a l'échelle de 1-2 m s^{-1}. Une étude de sensibilité similaire indique aussi que les techniques traditionnelles d'intégration vers le haut ne respectent pas les contraintes de continuité de masse. Une évaluation est aussi conduite en utilisant les radars profileurs de vent 915-MHz qui sont co-localisés. Le biais moyen et les erreurs absolues entre les deux méthodes sont a l'échelle de 0.5 m s^{-1} et 1 m s^{-1} respectivement avec corrélation en temps et hauteur a l'échelle de 0.5. Ces résultats sont encouragent et dans le futur pourrait produire de meilleurs ensembles de données d'observation pour contraindre les simulations numériques de convection.

TABLE OF CONTENTS

LIST OF TABLES

LIST OF FIGURES

CHAPTER 1
INTRODUCTION

1.1 Convective air motion insights

The representation of deep convection at cloud resolving and global circulation model scales (CRMs and GCMs) is an ongoing challenge [Jakob, 2010]. The slow advancement can be partially attributed to the lack of comprehensive observations of dynamics and microphysics in these vigorous cloud systems [Ferrier, 1994; Milbrandt and Yau, 2005; Mrowiec et al., 2012]. In particular, cloud dynamical insights may provide necessary guidance for improving these simulations to storm scales and act as a basis for improving convective parameterizations at GCM scales [Lang et al., 2007; Wu et al., 2009].

Despite the importance of vertical velocity measurements in deep convection, such measurements are not easy to collect. Traditionally, convective vertical velocity profiles have been measured directly by aircraft [Byers and Braham, 1948]. The measurements are accurate [Lenschow, 1976], but they are also collected under significant monetary cost and practical hazards associated with storm-penetrating aircraft operations. In particular, the practical hazards often limit available storm updraft and downdraft properties to those collected from flights within non-severe thunderstorms or tropical cumulus [LeMone and Zipser, 1980]. Long-term vertical air motion statistics collected from aircraft have also previously informed GCM parameterizations in more direct applications [Donner et al., 2001].

Profiling Doppler radars provide another avenue for acquiring vertical velocity insights in deep convective clouds. Many previous studies investigate convective cloud vertical air motion retrievals from ground-based [Atlas et al., 1973; Cifelli and Rutledge, 1994; May and Rajopadhyaya, 1999; Kollias et al., 1999; Williams, 2012; Giangrande et al., 2010, 2011, 2013a; Kumar et al., 2015] and airborne radar [Jorgensen and LeMone, 1989; Heymsfield et al., 2010]. Profiling radar methods typically rely on Doppler spectra signatures or dual-frequency techniques to deconvolve the ambient air motion contribution [Kollias et al., 1999; Williams, 2012; Luke and Kollias, 2013]. These methods also require information about the reflectivity-weighted fall velocity of the hydrometeor size distribution. Thus, an uncertainty of 1-2 m s^{-1} is expected in deep convective clouds with these methods [e.g., Atlas et al., 1973]. Compared to the true magnitude of updrafts and downdrafts in deep convective clouds (e.g., 10-20 m s^{-1}), profiling radar vertical velocity retrieval error is acceptable (e.g., 10%) and thus can be considered a viable substitute for aircraft measurements. Nevertheless, profiling radars share similar limitations to aircraft measurements given the narrow column volumes sampled by these radar.

1.2 Multi-Doppler radar wind retrievals

Wind retrievals from ground-based scanning Doppler radar networks may also help overcome known in situ aircraft and profiling radar limitations. One advantage is the potential to accumulate velocity statistics over extended areas in better alignment with CRM and GCM domains [e.g., Collis et al., 2013; Kumar et al., 2015]. Thus, in addition to improved statistics, this approach offers the ability to document the three-dimensional structure of updrafts and downdrafts. Traditional multi-Doppler wind retrieval techniques estimate vertical air motion using a mass continuity constraint applied to an estimate of the two-dimensional horizontal wind field which is more adequately sampled by scanning radars [e.g., Armijo, 1969; Lhermitte and Gilet, 1975; Ray et al., 1980; Laroche and Zawadzki, 1994; Protat and Zawadzki, 1999]. In this traditional framework, the explicit integration of mass continuity is required, contingent on *known* solutions of vertical velocity at bottom (e.g., bottom-up integration) or top (top-down integration) column boundaries. This technique shares elements with three-dimensional variational (3D-VAR) techniques (e.g., formally minimizing a cost function), but are known to produce suboptimal results by not satisfying all analysis constraints simultaneously [Bousquet and Chong, 1998; Dowell and Shapiro, 2003; Potvin et al., 2012b].

However, the use of scanning Doppler radar networks for retrieving the vertical air motion in convective clouds is challenging. First, distributed Doppler radar networks, including mobile radar deployments, designed to study the dynamics of deep convection, are not widely available or standardized. Operational networks such as the NEXRAD WSR-88D network tend to provide inadequate coverage from multiple angles necessary to properly constrain convective cloud wind retrievals. Several studies have investigated practical wind retrieval uncertainties by identifying or utilizing (1) the importance of Doppler radar measurement errors and beam geometry [e.g., Doviak et al., 1976; Nelson and Brown, 1987; Matejka and Bartels, 1998] (2) the influence of radar data objective analysis, including storm morphological considerations [e.g., Clark et al., 1980; Gal-Chen, 1982; Testud and Chong, 1983; Chong et al., 1983; Given and Ray, 1994; Majcen et al., 2008; Shapiro et al., 2010; Collis et al., 2010] and (3) observing system simulation experiments (OSSEs) [e.g., Fanyou and Jietai, 1994; Gao et al., 1999; Liou and Chang, 2009; Potvin and Wicker, 2012]. Few studies have explored practical wind retrieval performance to independent air motion estimates from aircraft or ground-based profiling radars [e.g., Collis et al., 2013].

Recent 3D-VAR techniques promise several advantages over the traditional counterpart due to their ability to simultaneously satisfy all available analysis constraints [Bousquet and Chong, 1998; Liou and Chang, 2009; Potvin and Wicker, 2012]. Most notably, the explicit integration of mass continuity is not required and as a result the concurrent accumulation of vertical velocity errors in the column is avoided [e.g., Ray et al., 1980]. A simultaneous 3D-VAR method can also mitigate retrieval instabilities that tend to form in ill-conditioned regions (e.g., near the radar baseline) known to affect traditional solutions [Bousquet and Chong, 1998; Dowell and Shapiro, 2003; Liou and Chang, 2009]. Furthermore, incorporating additional constraints like vorticity is naturally suited in this framework. Overall, it has been suggested that a simultaneous 3D-VAR method theoretically permits a more accurate wind retrieval from scanning Doppler radars than traditional methods [e.g., Bousquet and Chong, 1998; Dowell and Shapiro, 2003; Potvin et al., 2012a]. Herein, we adapt the terminology of Potvin et al. [2012a] and reserve 3D-VAR wind retrievals for representing simultaneous methods.

While 3D-VAR wind retrieval methods have been studied using OSSEs [e.g., Gao et al., 1999; Liou and Chang, 2009; Shapiro et al., 2009; Potvin et al., 2012a,b; Potvin and Wicker, 2012], an implementation, verification and sensitivity analysis on real datasets is noticeably missing. To this end, the ARM SGP site in Oklahoma provides an excellent opportunity to investigate the benefits and practical errors associated with multi-Doppler wind retrievals [Stokes and Schwartz, 1994; Mather and Voyles, 2012]. Recently, the ARM SGP site was upgraded to include the installation of an advanced radar network. The multi-Doppler wind retrievals presented in this study capitalize on the inaugural operation of this radar network. These data were collected during the Midlatitude Continental Convective Clouds Experiment (MC3E), a joint field campaign between the DOE ARM program and the National Aeronautics and Space Administration (NASA) Global Precipitation Measurement (GPM) mission Ground Validation (GV) program [Jensen et al., 2015]. This campaign featured the deployment of multiple radar wind profilers, each operating in a novel deep convective mode [Tridon et al., 2013; Giangrande et al., 2013a]. To the author's knowledge, this study reports the first time multiple profiling instruments have been optimally placed within a multi-Doppler scanning radar network to act as independent validation references for vertical air motion retrievals.

The remainder of this study is organized as follows. A description of the dataset and radar data processing is presented in Chapter 2. Chapter 3 provides a thorough discussion of variational wind retrieval methods from scanning Doppler radars. Chapter 4 presents the wind retrieval results in the context of how they compare with those from independent collocated radar wind profilers as well as with a traditional bottom-up method. Chapter 5 is reserved for summary and further discussion topics.

CHAPTER 2
DATASET AND RADAR PROCESSING

2.1 Midlatitude Continental Convective Clouds Experiment

The primary dataset used in this study was obtained during MC3E, which took place during April-June 2011 in Oklahoma and surrounding states. Creating a holistic view of continental convective cloud evolution was a primary science goal of MC3E. This involved the coordination of multiple sensors, including in situ aircraft observations, ground-based scanning cloud and precipitation radars, lidar and radiometer systems, and a comprehensive radiosonde and surface disdrometer network [Jensen et al., 2015]. The location of pertinent instruments around the ARM SGP Central Facility (CF) during MC3E are shown in Figure 2–1.

A total of five MC3E events were analyzed for this study and are listed in Table 2–1. The events represent a variety of warm season convection over Oklahoma, including nocturnal elevated convection (25 April 2011), widespread stratiform precipitation with embedded convection (11 May 2011), mesoscale convective system (MCS) and associated squall line (20 May 2011), and isolated severe supercell thunderstorms (23-24 May 2011). The time frame defining each event reflects profiling radar observations at the CF (see Section 2.3), specifically the longest continuous time frames where deep convection and associated stratiform precipitation were observed, and it does not necessarily correspond to the times where scanning radar observations were available.

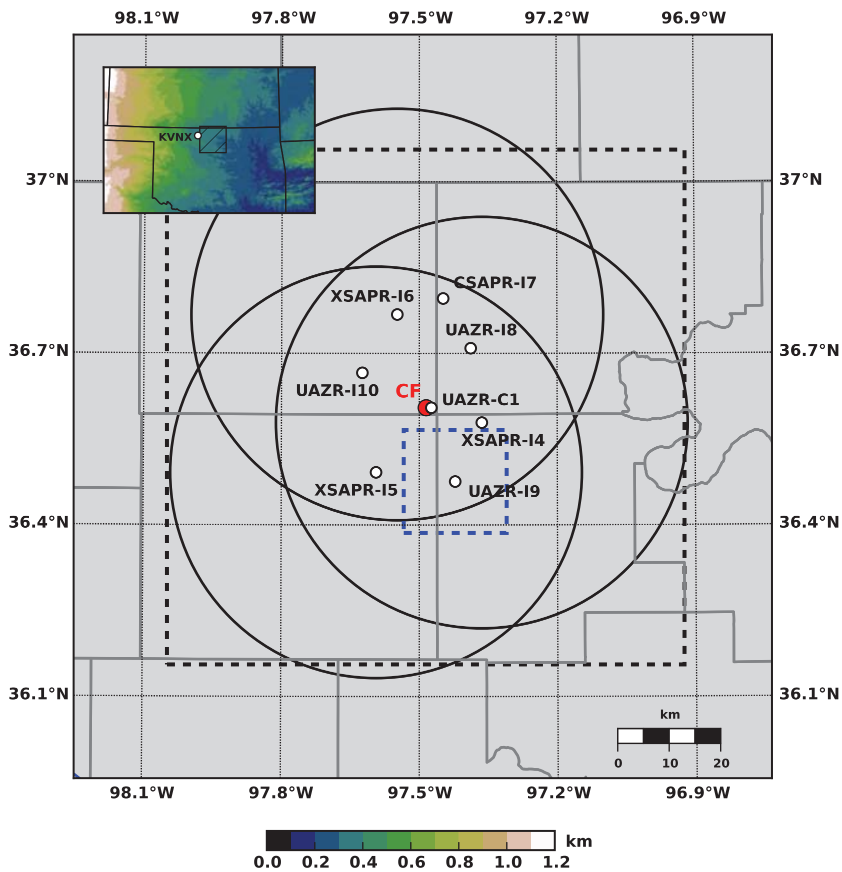

Figure 2–1: ARM SGP site with locations of relevant ARM and NEXRAD radar systems surrounding the Central Facility (CF). The dashed black box in the primary panel corresponds to the 100 km x 100 km multi-Doppler analysis domain, also shown in the inset panel. Radar range rings at 40 km (black circles) are shown for the three ARM X-band radars (XSAPRs) which indicates their maximum range (see Table 2–2). The ARM C-band radar (CSAPR-I7) is capable of covering the full area shown in the main panel. The separate analysis domain used in the sensitivity analysis (see Section 3.2) is shown as the dashed blue box surrounding the southeast radar wind profiler location (UAZR-I9). The inset panel provides the large-scale view of the region including the local topography in kilometers above mean sea level.

Table 2–1: Prominent convective events during MC3E, including a brief description of each event and approximate time frame each event was sampled by UAZR-C1.

Event	Description	Time frame (UTC)
25 Apr 2011	Isolated, elevated convection	0900-1030
11 May 2011	Isolated convection, widespread stratiform precipitation	1800-2300
20 May 2011	Mesoscale convective system, squall line	0600-1600
23 May 2011	Isolated, severe convection	2130-2300
24 May 2011	Isolated, severe convection	2100-2230

2.2 ARM scanning radar network

During the course of 2010 through early 2011, the ARM SGP site was upgraded with the installation of a network of scanning Doppler and dual-polarization radars in order to improve the mapping and understanding of clouds and precipitation over large domains (e.g., 100 km x 100 km) [Mather and Voyles, 2012]. The upgraded radar facility includes a 6.3-GHz C-band scanning ARM polarimetric radar (CSAPR) and three networked 9.4-GHz X-band scanning ARM polarimetric radars (XSAPRs). Their technical specifications are listed in Table 2–2. Since there were multiple volume coverage patterns (VCPs) designed for the ARM scanning radars during MC3E depending on the current or imminent convective outlook, Table 2–2 references the plan position indicator (PPI) convective mode settings of these radars. The convective mode was designed to adequately sample deep convective clouds often observed during the warm season in Oklahoma, including dense coverage in the atmospheric boundary layer (0-3 km AGL) and elevation scans upwards of 50 deg.

Table 2–2: Operational parameters of the ARM scanning X- and C-band radar network during MC3E when running in a plan position indicator (PPI) convective mode.

Parameter	XSAPR	CSAPR
Frequency (GHz)	9.4	6.3
Wavelength (cm)	3.2	4.8
PRF (kHz)	2.2	1.2
Pulse width (ns)	460	800
Nyquist velocity (m s^{-1})	16.8	16.5
3-dB beamwidth (deg)	1.2	1.0
Range resolution (m)	50	120
Temporal resolution (min)	5-6	6-7
Maximum range (km)	40	117
Number of elevations	22	17
Elevation range (deg)	0.5-50.1	0.5-42.0

The MC3E marked the first operational period of the ARM SGP scanning radar network, thus special care had to be taken with the raw data in order to address several common radar data issues and artifacts. Radar calibration for all events was supported by ARM and NASA GPM mission personnel. Reflectivity calibration for the ARM radars is expected to be within 1-2 dB and calibration efforts benefited from cross-validation with a suite of nearby surface disdrometers, profiling radars, and WSR-88D references [Giangrande et al., 2014]. The two most significant radar data artifacts affecting wind retrievals are ground clutter echoes and Doppler velocity aliasing. The majority of techniques for removing ground clutter involve conditional thresholding of various radar measurements, however these methods tend to have a high false classification rate [Rico-Ramirez and Cluckie, 2008]. Here, a naive Bayes classifier was developed in order to predict the likelihood a radar echo originated from either a meteorological scatterer or ground object. First, significant radar echoes, excluding those from ambiguous targets (e.g., second-trip echoes), were identified. This is a necessary step in order to eliminate all range gates characterized by noise from the conditional probability distributions necessary in Bayesian methods. Manual inspection of a variety of remote sensors was utilized in order to identify a set of radar volumes that primarily contained either hydrometeor (meteorological) or ground clutter echoes. In this study, a radar volume was identified as a ground clutter volume if it contained no significant biological (e.g., insects and birds) or Bragg echoes. These volumes were used to develop the calibration datasets for the Bayes classifier. Following the notation of Rico-Ramirez and Cluckie [2008], the naive Bayes classifier can be expressed as,

$$P(c|x_1, \ldots, x_n) = \frac{P(c) \prod_{i=1}^{n} P(x_i|c)}{P(x_1, \ldots, x_n)}, \tag{2.1}$$

where c and $x_1, \ldots, x_n$ are the class and the n radar input measurements, respectively. It follows that c represents either the meteorological or ground clutter class. $P(c|x_1, \ldots, x_n)$ is the joint probability model, expressing the probability of the class c given the n radar inputs, and $P(x_i|c)$ represents the conditional probability of each radar input x_i given class c. Since $P(x_1, \ldots, x_n)$ is class independent it is effectively constant and therefore set to 1 for convenience. $P(c)$ represents the probability of the class c and as a result is dependent on the calibration dataset, specifically its sample size for each class. To remove any sampling bias, $P(c)$ is assumed equally likely for both classes. The product in (2.1) implies that information can effectively be lost if the conditional probability of one or more radar inputs is zero for a given radar measurement, therefore we specify a minimum *zero* probability of 1×10^{-3}. Radar Doppler moments, polarimetric measurements, and texture fields are used as the inputs, texture fields being defined as the standard deviation of a radar measurement within a predefined two-dimensional azimuth-range window [e.g., Cho et al., 2006; Gourley et al., 2007; Rico-Ramirez and Cluckie, 2008]. A total of $n = 13$ radar inputs are used to classify radar echoes: reflectivity Z_H, Doppler velocity and spectrum width, normalized coherent power, copolar correlation coefficient ρ_{HV}, differential reflectivity Z_{DR}, as well as the texture fields of those measurements listed including total differential phase shift Ψ_{DP}.

The calibration datasets are used to build up the conditional probabilities $P(x_i|c)$, an example of which from XSAPR-I4 volumes is given in Figure 2–2 for select inputs. A total of 152 meteorological and 338 ground clutter volumes spanning multiple days and times of day during MC3E were used to build up the occurrence statistics in Figure 2–2. A 3 x 3 azimuth-range window was used to compute the texture fields for all volumes. If less than 5 radar gates were occupied by a significant detection in the azimuth-range window than the texture field was considered undefined. The less overlap between the two class distributions, the less likely a false classification is made. From this it follows that some radar inputs are better than others at discriminating echo sources. For example, Ψ_{DP}, Z_{DR}, and ρ_{HV} texture fields have little overlap in their class distributions and therefore can be good discriminators between meteorological and ground clutter echoes. On the other hand Z_H alone is a poor discriminator due to the large overlap between its

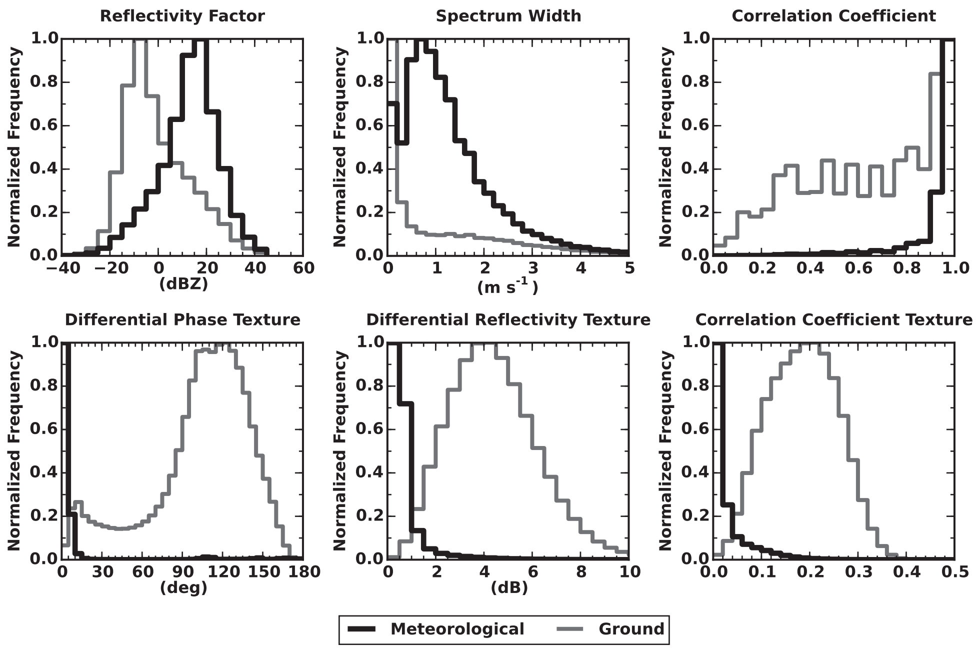

Figure 2–2: Normalized frequencies for select radar measurements and texture fields derived from XSAPR-I4 volumes. From left to right: reflectivity Z_H, Doppler spectrum width, copolar correlation coefficient ρ_{HV}, total differential phase Ψ_{DP} texture, differential reflectivity Z_{DR} texture, and ρ_{HV} texture. Texture fields are computed using a 3 x 3 azimuth-range window. The normalization factor is the maximum frequency observed for each class.

class distributions. A conditional threshold of $\rho_{HV} \leq 0.7$ is often used to identify and remove ground clutter echoes in dual-polarization radar data, and this is reinforced in Figure 2–2 where the meteorological distribution quickly drops off past 0.95 with effectively no occurrences past 0.7. However, this threshold does not account for the large occurrences of ρ_{HV} between 0.8 and 1.0 for ground clutter, in fact the ground clutter distribution has a maximum at $\rho_{HV} = 1$ similar to the meteorological class, therefore several radar gates would likely be misclassified as meteorological instead of ground clutter using a conditional ρ_{HV} threshold. Finally, the widths of the texture field distributions for the ground clutter class are all considerably larger than their meteorological counterparts, implying that ground clutter tends to look highly variable on PPI and other radar displays.

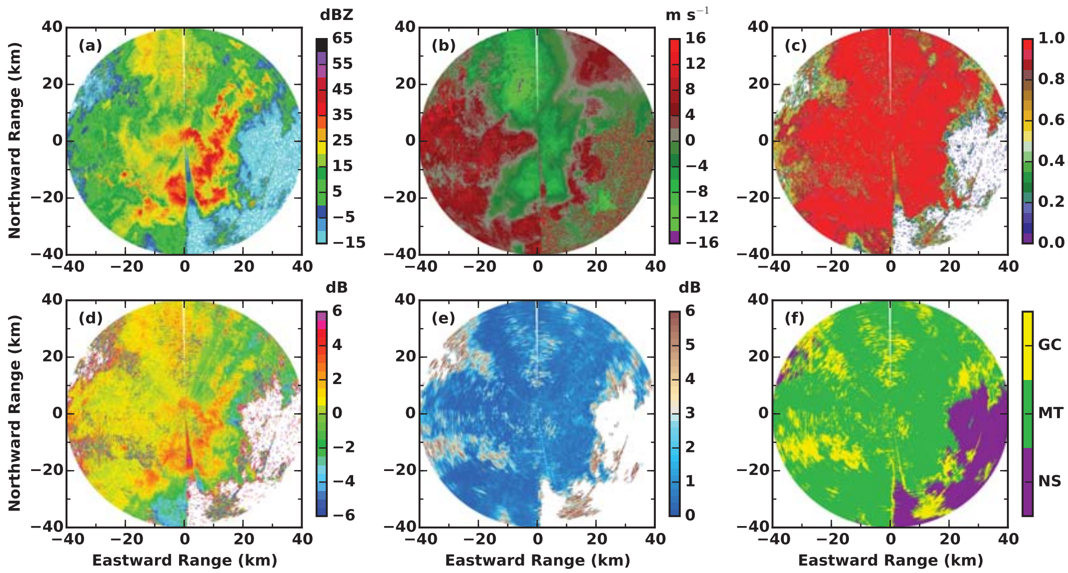

Figure 2–3: Example of raw (a) reflectivity Z_H (b) Doppler velocity (c) copolar correlation coefficient ρ_{HV} (d) differential reflectivity Z_{DR} (e) Z_{DR} texture field and (f) corresponding radar echo classification from the 0.5 deg elevation scan of XSAPR-I4 near 1900 UTC on 11 May 2011. The echo classification labels correspond to no scatterer (NS), meteorological (MT), and ground clutter (GC).

An example of using the occurrence statistics of Figure 2–2 and equation (2.1) to classify radar echoes is shown in Figure 2–3. The 0.5 deg elevation data is from XSAPR-I4 observations of a widespread precipitation event with embedded convection near 1900 UTC on 11 May 2011. As shown, during times of heavy precipitation ground clutter can become embedded in the meteorological echoes. Furthermore, it is difficult to visually identify the ground clutter echoes from the Z_H and Doppler velocity data in Figure 2–3a-b alone. The zero-Doppler velocity region of the precipitation covers a wide area, meaning a conditional Doppler velocity threshold near 0 m s^{-1} would falsely classify a large number of precipitation echoes. The polarimetric data in 2–3c-d provides additional information for making a better classification. The areas in the scan where ρ_{HV} and Z_{DR} are both highly variable (large texture values) likely indicates the echoes originate from ground objects as determined by the occurrence statistics in Figure 2–2. The echo classification results in Figure 2–3f ultimately show the necessity to accurately classify radar echoes due to the large number of ground clutter echoes that can still contaminate heavy precipitation events. These methods and results have been applied to the other ARM XSAPR and CSAPR systems.

After radar echoes were classified and non-meteorological echoes removed, additional radar processing steps included a standard dual-polarization reflectivity correction for attenuation in rain appropriate for the ARM C-band radar [Bringi and Chandrasekar, 2001; Giangrande et al., 2013b, 2014]. Additionally, the relatively low XSAPR and CSAPR Nyquist velocities ($\sim$ 16 m s^{-1}) meant that significant Doppler velocity aliasing would likely be a factor when sampling convective cloud air motions, where horizontal velocities can easily exceed 30 m s^{-1}. Doppler (radial) velocities were corrected for aliasing using the four-dimensional technique described in James and Houze [2001]. Similar to Collis et al. [2013], this technique was applied iteratively to further mitigate aliased regions. First, multiple wind profiles from the MC3E radiosonde network were used as initial conditions to generate a first-pass radial velocity field. The first-pass velocity field then served as the initial conditions for a second pass which incorporated a previously corrected radar volume. If no previously corrected radar volume existed, then the first-pass results were used. Finally, the performance of this routine was manually verified for each radar volume to check for potential errors and artifacts. All three steps were often necessary to ensure a radial velocity field absent of significant issues.

Following all processing and quality control routines, which were done in the native radar polar coordinates, radar data were mapped to a common Cartesian analysis domain. This study employs a domain that covers 100 km x 100 km x 10 km in meridional, zonal, and vertical extent, respectively. The horizontal area covered by the grid approximately encloses all available XSAPR data as shown in Figure 2–1, with the SGP Central Facility located at the origin. Each grid dimension has a constant resolution of 250 m. The terrain covered by the analysis domain is relatively flat, with the surface elevation varying less than 30 m over the entire domain. Therefore, this study neglects nuances associated with complex terrain [e.g., Chong and Cosma, 2000; Liou et al., 2011]. Radar data mapping was accomplished using a one-pass isotropic Barnes distance-dependent weighting function with a constant smoothing parameter of 2.98 km^2 [Barnes, 1964; Trapp and Doswell, 2000]. Several choices of weighting functions and their free parameters are found throughout the literature [e.g., Pauley and Wu, 1990; Askelson et al., 2000, 2005; Askelson and Straka, 2005; Trapp and Doswell, 2000; Collis et al., 2010], however the weighting function used in this study is desirable for the preservation of the input radar data phase and amplitude, as well as its relative insensitivity to the spatial characteristics of the input data [Trapp and Doswell, 2000].

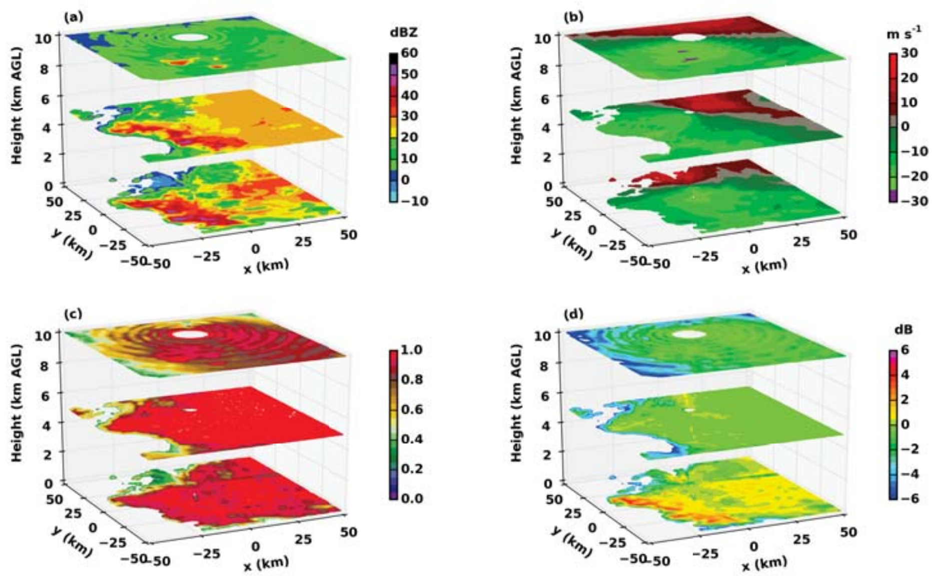

Figure 2–4: Example of mapped CSAPR-I7 data from a volume scan on 20 May 2011 (a) reflectivity Z_H (b) Doppler (radial) velocity (c) copolar correlation coefficient ρ_{HV} and (d) differential reflectivity Z_{DR}. Cross sections at 0 km (surface), 5 km, and 10 km AGL are shown in each panel. The grid domain corresponds to that shown in Figure 2–1, with the ARM SGP Central Facility at the origin.

An example of mapped CSAPR-I7 data from a volume scan on 20 May 2011 is shown in Figure 2–4. The more intense convective cells seen in the reflectivity field in Figure 2–4a to the southwest of the CF extend throughout the troposphere, with tops past 10 km AGL. Outflow from these cells as well as others in the region covers much of the analysis domain at heights above 5 km AGL. Some common gridding artifacts can be seen in the 10 km cross sections, most notably the CSAPR-I7 cone of silence and related sampling artifacts. Low signal-to-noise ratios can further enhance these artifacts. While data at these heights are generally suboptimal and can lead to vertical velocity retrieval errors on the order of 2 m s^{-1} [e.g., Collis et al., 2010], it still adds necessary value within a network of scanning radars.

2.3 ARM 915-MHz radar wind profilers

Four 915-MHz UHF-band ARM zenith-pointing radar wind profilers (UAZRs) were optimally placed within the scanning radar domain, their locations also shown in Figure 2–1 [Tridon et al., 2013; Giangrande et al., 2013a]. Additional details about the radar wind profilers running in their novel convective mode are described in Table 2–3. The long-mode is designed to suitably sample the depth of Oklahoma convective clouds with a 20 m s^{-1} Nyquist velocity sufficiently large enough to capture the most intense convective updrafts and downdrafts. Due to its long pulse width however, the long-mode can saturate the radar receiver at range gates near and below 1 km AGL, therefore the short-mode was introduced to mitigate these issues. Vertical air motion retrievals from the wind profilers follow the methods outlined by Giangrande et al. [2013a] and are assumed accurate to within 2 m s^{-1} in deep convective updrafts and downdrafts.

An example of UAZR observations of convective clouds observed on 25 Apr 2011 and the corresponding vertical air motion retrieval are shown in Figure 2–5. Running in convective mode, the UAZRs have a minimum detectable signal of approximately 5 dBZ at 10 km AGL and thus are not sensitive to typical

Table 2–3: Operational parameters of the ARM 915-MHz radar wind profilers (UAZRs) during MC3E running in a novel convective mode.

Parameter	Short-mode	Long-mode
Frequency (MHz)	915	–
Wavelength (cm)	33	–
PRF (kHz)	10.0	8.3
Pulse width (ns)	400	2833
Maximum range (km)	9.3	15.0
Nyquist velocity (m s^{-1})	14.7	20.0
3-dB beamwidth (deg)	9	–
Range resolution (m)	120	200
Native temporal resolution (s)	3	–
Resampled temporal resolution (s)	6	–

ice clouds above this level. The resolvable dynamical scales of the UAZRs are inherently different than that of the scanning ARM radars, therefore perfect correlations and magnitudes between the two datasets are not expected. For example, the small scale (e.g., 2-4 minutes) upwards and downwards air motions visible in Figure 2–5d between 1000-1040 UTC near 2 km AGL are unresolvable by a scanning radar network sampling similar volumes every 6-7 minutes. The updraft feature near 1020 UTC with a depth of approximately 4 km has the potential to be resolved by a scanning radar network due its larger time-height extent and overall intensity, likely forced by larger-scale air convergence. Section 4.1 further discusses the steps taken in this study to match the profiling and scanning radar datasets.

2.4 NEXRAD WSR-88D network

The WSR-88D radar network consists of over 150 2.8-GHz (10.7 cm) S-band scanning Doppler radars throughout the contiguous United States. All

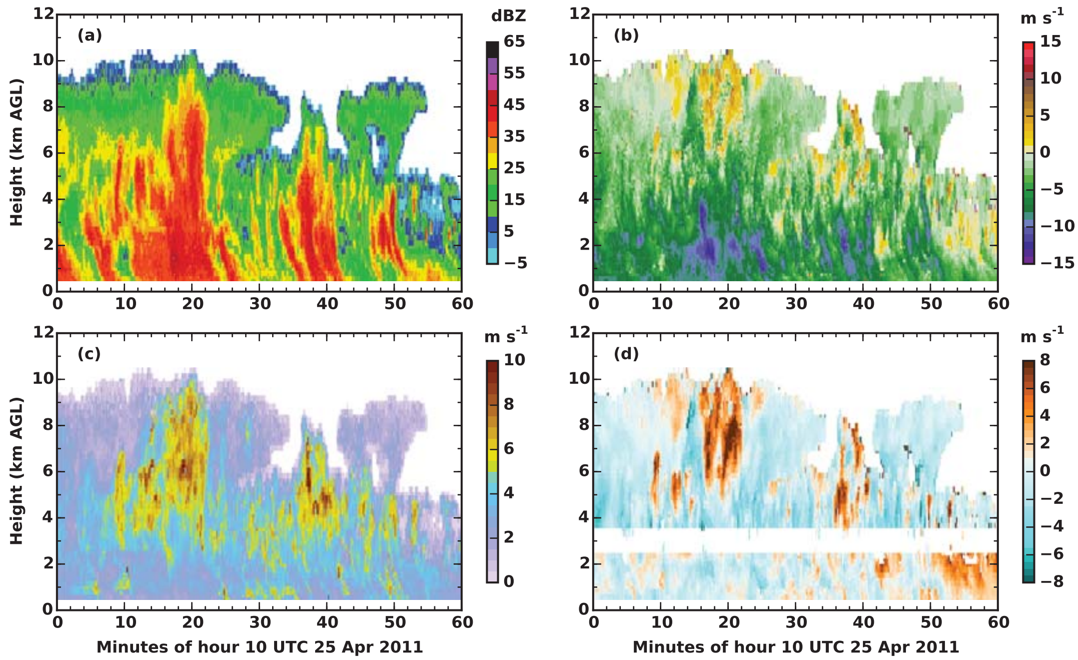

Figure 2–5: Example (a) reflectivity (b) Doppler velocity (c) spectrum width and (d) corresponding vertical air motion retrieval for UAZR-C1 on 25 Apr 2011. Vertical air motion within the melting layer (2.5-3.5 km AGL) was not retrieved for this event.

wind retrievals presented in this study benefit from the inclusion of WSR-88D observations due to the minimal attenuation in rain at S-band. This is especially true for the 11 May 2011 case, when CSAPR-I7 was not operational and the WSR-88D radar reflectivity was available and superior to the XSAPR reflectivity observations. WSR-88D radars are run in a unique convective mode when heavy precipitation and convection are within range. Furthermore, NEXRAD Level II data are relatively artifact free aside from Doppler velocity aliasing, therefore after running the velocity correction routine described in Section 2.2, these data were mapped to the same Cartesian grid as the ARM radars.

The closest WSR-88D site to the SGP CF is Vance Air Force Base (KVNX), located approximately 56 km west of the CF. This relatively large distance, coupled with the 0.5 deg base elevation scan of KVNX, ensures that its transmitted pulses are already close to 1 km above the surface for grid points near the CF. Figure 2–6 illustrates the closest distance D a radar range gate is to each grid point in the analysis domain (herein gate-grid distance). Each gate-grid distance in Figure 2–6 is computed assuming standard atmospheric refraction (e.g., 4/3 Earth's radius model) [Doviak and Zrnić, 1993]. The circular features seen in most cross sections are a result of the PPI scanning pattern of each radar, which can be characterized as dense in the lower troposphere (0-5 km AGL), becoming sparser in the upper troposphere. The ARM scanning radars show superior spatial coverage over the CF (darkest blue shades), especially below approximately 5 km AGL. The spatial coverage near the surface from the ARM radars is especially ideal for atmospheric boundary layer characterization, with gate-grid distances typically less than 150 m at heights below 3 km AGL. In contrast, KVNX has relatively poor spatial coverage near the surface, with $D > 800$ m for most grid points in Figure 2–6. However, at heights above 5 km AGL, KVNX adds significant observational value, especially for grid points close to and directly over XSAPR-I4 and other ARM scanning radars. The dark red shades ($D \geq 2$ km) seen in the 6 km and 10 km AGL XSAPR-I4 panels highlights the radar cone of silence, a measurement gap due to no elevation scans past 50 deg (see Table 2–2). Essentially, Figure 2–6 emphasizes the need to consider variable weighting of scanning radar observations. For example, a larger weight should be given to ARM scanning radar observations over KVNX observations near the surface. To accomplish this, scanning radar observation weights are modeled as an exponential decay contingent on the gate-grid distance D. For further details see Section 3.1.

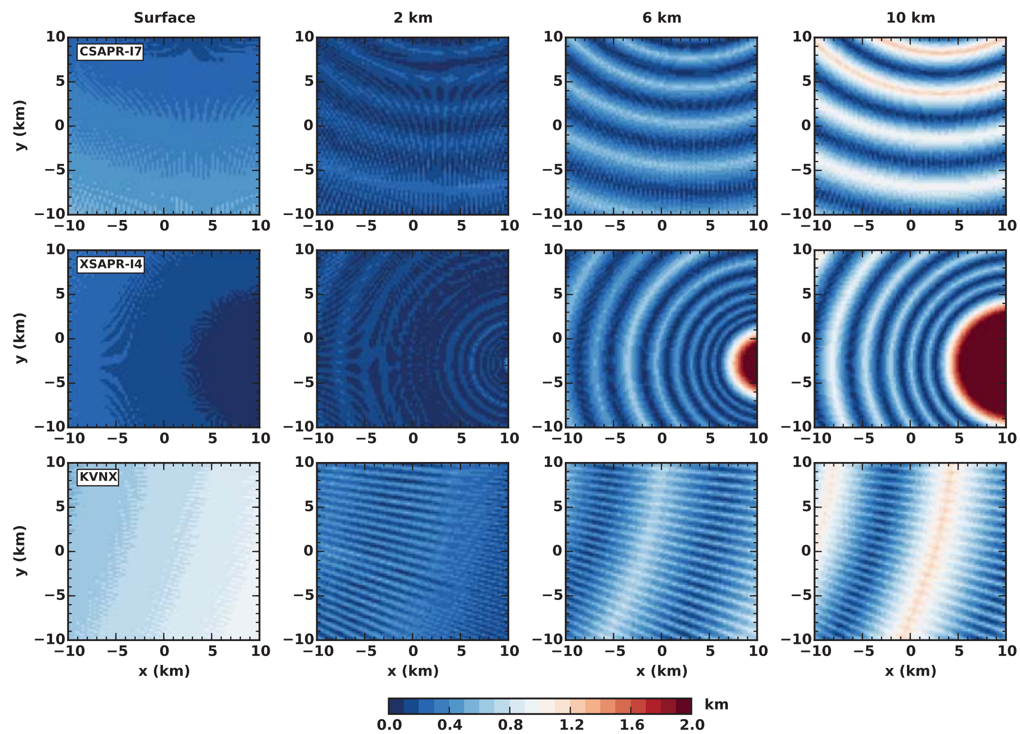

Figure 2–6: Gate-grid distances D within 20 km x 20 km surrounding the ARM SGP CF for select radars and horizontal cross sections of 0 km (surface), 2 km, 6 km, and 10 km AGL.

CHAPTER 3
METHODOLOGY

3.1 Variational wind retrievals

The variational calculus [Sasaki, 1970] has a long history in ground-based single and multi-Doppler radar wind retrievals [e.g., Ray et al., 1980; Scialom and Lemaître, 1990; Laroche and Zawadzki, 1994; Bousquet and Chong, 1998; Protat and Zawadzki, 1999, 2000; Shapiro and Mewes, 1999; Gao et al., 1999; Lui et al., 2005; Bousquet et al., 2008; Shapiro et al., 2009; Potvin et al., 2012a]. An optimal wind field solution is found by combining multiple sources of information within a single cost function and minimizing the variance of each information source. As discussed in Section 1.2, traditional methods do not evaluate all sources of information simultaneously. For results presented in this study, Doppler (radial) velocity observations J_o, anelastic mass continuity J_c, spatial smoothness J_s, a background field J_b, and surface impermeability J_p are used as weak constraints to produce an optimal estimate of the meridional $\mathbf{u}$, zonal $\mathbf{v}$, and vertical $\mathbf{w}$ Cartesian wind components following

$$J = J_o + J_c + J_s + J_b + J_p. \tag{3.1}$$

The optimal wind field solution is at the (global) minimum of J, which implies the gradient of J with respect to $\mathbf{u}$, $\mathbf{v}$, and $\mathbf{w}$ vanishes. For applications requiring large-scale (e.g., 10^6 variables) nonlinear cost function minimization, it is often necessary to use an iterative conjugate-gradient method [Navon and Legler, 1987]. Therefore, a Polak and Ribiere [1969] based conjugate-gradient method is used to minimize (3.1). As will be shown, each individual cost in (3.1) is weighted by a single or multiple coefficients designed to indicate its relative importance on the wind field solution. These coefficients are typically treated as adjustable parameters, their values often determined through trial and error [e.g., Gao et al., 1999].

The radial velocity observation constraint in (3.1) for a single radar is

$$J_o = \frac{1}{2} \sum_{i,j,k} \lambda_o \left(V_r - V_{r,o} \right)^2 . \tag{3.2}$$

The summation is over all Cartesian grid points in the analysis domain. A summation is used to represent J_o rather than a volume integral because the multi-Doppler analysis domain has been discretized. In (3.2), λ_o is the radial velocity observation weight, $V_{r,o}$ is the observed radial velocity from the radar, and V_r is the projected radial velocity of the wind field onto the radar's line of sight, computed using simple geometrical considerations as in Ray et al. [1980]. Implicit in V_r is an estimate of hydrometeor fall speed. For this study, the hydrometeor fall speed is estimated using an empirical relationship involving the radar reflectivity [Caya, 2001]. Generally the radial velocity observation weight is set to a nonzero constant value (e.g., $\lambda_o = 1$) where radial velocity observations exist, and $\lambda_o = 0$ otherwise [Gao et al., 1999; Shapiro et al., 2009; Potvin et al., 2012a]. However, not all observations should be treated equal, as shown in Figure 2–6 and corresponding discussion in Section 2.4. Instead, the observation constraint weight for each radar is modeled as an exponential decay dependent on the gate-grid distance D,

$$\lambda_o = \hat{\lambda}_o \exp\left(-\lambda \frac{D - D_{\min}}{D_{\max} - D_{\min}}\right), \tag{3.3}$$

where $D_{\min}$ is the minimum radar gate-grid distance, which for all radars is approximately 0 km, and $D_{\max}$ is a maximum distance defined by the chosen distance-dependent weighting function. The Barnes weighting function behavior presented in Section 2.2 approaches zero when radar gates are approximately 5 km from a grid point, and beyond that distance the weight is effectively zero. Thus, we set $D_{\max} = 5$ km. In (3.3), $\hat{\lambda}_o$ controls the maximum observation weight possible. Without loss of generality, and to be consistent with the literature, we set $\hat{\lambda}_o = 1$. Finally, λ defines the minimum observation constraint weight possible, and for results presented in this study the weight equals 1% of its maximum value when $D = D_{\max}$.

Radial velocity observations used in (3.2) are collected from two or more radars sampling similar cloud volumes. These volumes are assumed to be closely matched in time. It is required that (a) both KVNX and CSAPR-I7 must be available (except 11 May 2011) and initiate a volume scan within 2 minutes from each other, and (b) any complementary XSAPR input must have initiated from a volume scan 2 minutes or less from either KVNX or CSAPR-I7. The choice of these criteria ignores the issues associated with cloud system advection and evolution [e.g., Gal-Chen, 1982; Shapiro et al., 2009]. Although temporal coordination of the ARM radar network was a high priority during the MC3E, select failures caused large temporal mismatches in radar sampling such that no wind retrieval was attempted.

Depending on whether a 3D-VAR or traditional solution is desired, the anelastic mass continuity constraint J_c in (3.1) is given by

$$J_c = \begin{cases} \dfrac{1}{2} \displaystyle\sum_{i,j,k} \lambda_c L^2 \left(\dfrac{\Delta u}{\Delta x} + \dfrac{\Delta v}{\Delta y} + \dfrac{\Delta w}{\Delta z} + \dfrac{w}{\rho} \dfrac{\Delta \rho}{\Delta z} \right)^2, & \text{if 3D-VAR} \\ \dfrac{1}{2} \displaystyle\sum_{i,j,k} \lambda_c \left(w - w_c \right)^2, & \text{if traditional,} \end{cases} \tag{3.4}$$

where λ_c is the continuity weight. For the 3D-VAR method, L is a length scale designed to unify the dimensions and magnitude of J_c with J_o [Legler and Navon, 1991; Bousquet and Chong, 1998]. Shapiro et al. [2009] incorporates a similar multiplier responsible for addressing a number of factors (e.g., the spatial gradient of $V_{r,o}$). However, for the retrievals presented in this study, $L = \Delta(x, y, z) = 250$ m. The traditional method does not require the scaling factor L because J_c has dimensions that are consistent with J_o. The anelastic mass continuity equation is written using the finite difference operator Δ to indicate that it has also been discretized. Air density ρ is required for both methods, and is derived from the MC3E radiosonde network and equation of state for dry air. For the traditional method, w_c is the vertical velocity computed from integrating the anelastic mass continuity equation either upwards (bottom-up), downwards (top-down), or a weighted average of both directions [e.g., Protat and Zawadzki, 1999]. For an upwards integration direction, w_c at the kth vertical level is given by,

$$\rho_k w_{c_k} = \rho_{k-1} w_{k-1} - \int_{z_{k-1}}^{z_k} \rho \left(\frac{\Delta u}{\Delta x} + \frac{\Delta v}{\Delta y} \right) \Delta z \tag{3.5}$$

Note the strict dependence on horizontal wind divergence in (3.5) and the fact that it must be known throughout the column before an estimate of vertical air motion can be made. As a result, any errors in horizontal wind divergence necessarily accumulate upwards, making w_c increasingly suspect with increasing height. The vertical extent of the analysis domain controls the possible integration directions for traditional methods. If the vertical extent of the cloud system is not adequately contained within the analysis domain, a top boundary condition becomes difficult to define, making top-down integrations unreliable. For warm season Oklahoma convective clouds, a domain extending upwards of 15 km AGL is typically necessary in order to use a top-down integration direction, however these heights are poorly sampled by the ARM radar network and therefore poorly constrained by observations (e.g., see Figure 2–6). Inadequate sampling aloft can lead to severe gridding artifacts which introduces spurious air motion retrievals at these heights [Collis et al., 2010]. This is the primary reason for capping the analysis domain at 10 km AGL (see Section 2.2). As a result, any traditional wind retrievals presented in the following sections are derived strictly from bottom-up integrations following (3.5).

The smoothness constraint J_s in (3.1) is designed to dampen small-scale (high frequency) fluctuations in the wind retrieval. Similar to Potvin et al. [2012a], we define this constraint as,

$$
\begin{aligned}
J_s \quad = \quad & \frac{1}{2}\sum_{i,j,k}\lambda_{s1}L^4\left[\left(\frac{\Delta^2 u}{\Delta x^2}\right)^2+\left(\frac{\Delta^2 v}{\Delta x^2}\right)^2+\left(\frac{\Delta^2 u}{\Delta y^2}\right)^2+\left(\frac{\Delta^2 v}{\Delta y^2}\right)^2\right]+\\
+ \quad & \frac{1}{2}\sum_{i,j,k}\lambda_{s2}L^4\left[\left(\frac{\Delta^2 u}{\Delta z^2}\right)^2+\left(\frac{\Delta^2 v}{\Delta z^2}\right)^2\right]+\\
+ \quad & \frac{1}{2}\sum_{i,j,k}\lambda_{s3}L^4\left[\left(\frac{\Delta^2 w}{\Delta x^2}\right)^2+\left(\frac{\Delta^2 w}{\Delta y^2}\right)^2\right]+\\
+ \quad & \frac{1}{2}\sum_{i,j,k}\lambda_{s4}L^4\left[\left(\frac{\Delta^2 w}{\Delta z^2}\right)^2\right],
\end{aligned}
\tag{3.6}
$$

where λ_{s1}, λ_{s2}, λ_{s3}, and λ_{s4} are the four unique smoothness weights designed to allow for differing smoothness impacts depending on the wind component and dimension. In addition to reducing retrieval noisiness, J_s is able to extrapolate the wind field solution into data-sparse or poorly constrained regions. For instance, smoothing may encourage usable solutions along the dual-Doppler radar baseline, or add value to regions directly above a radar where observations are limited or simply nonexistent [Bousquet and Chong, 1998].

The background constraint J_b accounts for discrepancies between the wind field and the background wind field. The general form of the background constraint can be written as

$$
J_b = \frac{1}{2}\sum_{i,j,k}\left[\lambda_{u,b}\left(u-u_b\right)^2+\lambda_{v,b}\left(v-v_b\right)^2+\lambda_{w,b}\left(w-w_b\right)^2\right], \tag{3.7}
$$

where $\lambda_{u,b}$, $\lambda_{v,b}$, and $\lambda_{w,b}$ are the background weights corresponding to their respective wind components u_b, v_b, and w_b. The background u_b, v_b, and w_b are typically derived from radiosonde profiles. For this study, wind retrievals utilize horizontally homogeneous wind profiles derived from the MC3E radiosonde network. Since vertical air motion estimates are not available from these radiosonde profiles, we ignore the vertical component in (3.7) by setting $\lambda_{w,b} = 0$. Furthermore, since u_b and v_b are assumed to be free of systematic errors, we set $\lambda_{u,b} = \lambda_{v,b} = \lambda_b$. Incorporating a background constraint helps promote a wind field solution in data-sparse regions based on additional observations, and coupled with the smoothness constraint J_s, can produce a realistic and aesthetically pleasing wind retrieval in regions where radial velocity observations are limited [Gao et al., 1999].

The final constraint in (3.1) is an appeal to surface impermeability, and is only applicable when the simultaneous method in (3.4) is used since the traditional method necessarily requires defining a bottom boundary condition. The surface impermeability constraint is written as

$$J_p = \frac{1}{2} \sum_{i,j,k} \lambda_p w^2, \tag{3.8}$$

where λ_p is the surface impermeability weight. This constraint is only applicable for surface grid points in the summation, and is set to zero everywhere else. The surface impermeability constraint is treated as a pseudo strong constraint by setting λ_p such that the retrieved vertical wind component at the surface effectively vanishes. For results shown in this study we set $\lambda_p = 1000$.

Similar to Collis et al. [2013], we adopt a two-pass technique to retrieval the wind field. The first pass uses a zero wind field as its first guess and performs a heavily smoothed retrieval designed to characterize the large-scale **u** and **v** flow while neglecting a retrieval of $\mathbf{w}$. The retrieved $\mathbf{u}$ and $\mathbf{v}$ from the first pass is used as an improved initial condition for the final pass, which retrieves all three wind components. In the OSSE of Gao et al. [1999], which used a similar cost function and conjugate-gradient minimization technique, the horizontal wind components were generally well recovered within the first 50 iterations of the minimization, however the vertical wind component lacked both coherency and strength. By iteration 200, the vertical wind component was adequately recovered. These values act as a baseline for the minimum number of iterations we require during the minimization of (3.1) for the final pass.

3.2 Practical wind retrieval sensitivity analysis

As introduced in equations (3.2-3.8), variational wind retrievals depend on several free parameters, the individual constraint weights (λs) used to indicate the relative impact each constraint should have on the wind retrieval. We refer to the range of possible constraint weights as the parameter space. In-depth sensitivity analysis for the selection of these weights is often ignored or not explicitly discussed primarily because studies typically consider theoretical wind retrieval performance by comparing it to a known *truth* field (e.g., model output in an OSSE). These studies adopt the weights that minimize the residual errors between the retrieved wind field and the truth wind field [e.g., Gao et al., 1999; Potvin et al., 2012b]. For applications involving real radar datasets as opposed to synthetic ones used in OSSEs, one must consider (i) determining a reasonable parameter space when no truth field is available and (ii) characterizing the wind field solution spread (uncertainty) within the parameter space determined by (i). This section considers these two points through an extensive sensitivity analysis within the experimental domain indicated by the dashed blue box in Figure 2–1. The experimental domain covers 20 km x 20 km horizontally and extends to 10 km in height. The grid resolutions are consistent with those of the larger domain discussed in Section 2.2. The reasons for selecting a smaller experimental domain for the sensitivity analysis include reducing processing time, allowing for thousands of wind retrievals to be processed, as well as the ability to isolate specific cloud type regimes within the smaller domain, those being convective versus stratiform clouds. Since convective velocity retrievals are the primary interest of this study, the sensitivity analysis is done during a time the experimental domain was characterized by deep convection on 23 May 2011, using scanning radar observations valid between 2236-2243 UTC.

To address (i) and (ii), we reduce the problem down to the following two questions. The first is *how well are the radial velocity observations satisfied?*. The second is *how well is anelastic mass continuity satisfied?*. The second question is particularly important from a convective parameterization and numerical modeling standpoint. Both questions are well posed in the sense that they have clear and direct answers. Furthermore, they allow us to adequately characterize the parameter space necessary to produce robust wind retrievals, as will be shown. Unless otherwise indicated, the baseline or nominal values for the constraint weights are those quoted in previous OSSE studies, namely the background constraint weights of Gao et al. [1999] and the smoothness constraint weights of Potvin et al. [2012b] (see Table 3–1).

The design of equation (3.2) is to produce a wind field that does not diverge from the radar $V_{r,o}$ observations. It follows that the root mean square error between the retrieved wind field V_r and the radar $V_{r,o}$ observations should not greatly exceed the uncertainty estimate of the actual radar observations. Conversely, a wind retrieval wherein this residual approaches 0 m s^{-1} is undesirable since there are inherent errors in $V_{r,o}$ associated with the raw measurements themselves (e.g., hardware noise and beamwidth effects) and the mapping from discrete sampling locations to a uniform Cartesian grid. Since it is impractical to account for all of the various error sources of $V_{r,o}$ and characterize this uncertainty either as a function of range or with a single value, we establish a range of acceptable values and strive for a wind retrieval that produces a root mean square error (RMSE) which falls within this range. For the ARM SGP scanning radar network, raw $V_{r,o}$ measurement errors can be as high as 0.5 m s^{-1} in regions of low signal-to-noise ratio and large spectrum width. However, mapping these discrete measurements onto a uniform Cartesian grid will introduce additional uncertainties, a conservative estimate being an additional 1 m s^{-1}. Therefore, an acceptable $V_{r,o}$ RMSE range is [0.5, 1.5] m s^{-1}.

Anelastic mass continuity is known to be a reasonable assumption in deep convective clouds [e.g., Ogura and Phillips, 1962; Lipps, 1990]. As a result, the retrieved wind field should satisfy anelastic mass continuity to a satisfactory degree throughout the entire analysis domain. Here we define the relative mass continuity residual as the ratio of squared anelastic mass continuity residual to the sum of squares of each individual term in the anelastic mass continuity equation. At the ith grid point, this is expressed as,

$$\alpha_i = \frac{\left(\frac{\Delta u}{\Delta x} + \frac{\Delta v}{\Delta y} + \frac{\Delta w}{\Delta z} + \frac{w}{\rho}\frac{\Delta \rho}{\Delta z}\right)_i^2}{\left(\frac{\Delta u}{\Delta x}\right)_i^2 + \left(\frac{\Delta v}{\Delta y}\right)_i^2 + \left(\frac{\Delta w}{\Delta z}\right)_i^2 + \left(\frac{w}{\rho}\frac{\Delta \rho}{\Delta z}\right)_i^2}. \tag{3.9}$$

As α approaches zero, anelastic mass continuity becomes perfectly satisfied, however this is not necessarily desirable since it is still an underlying assumption. Therefore, a reasonable range for the mean of α over the entire analysis domain would be [1%, 10%] when expressed as a percentage.

The response of CSAPR-I7 $V_{r,o}$ RMSE and relative continuity residual α to perturbing multiple 3D-VAR constraint weights is analyzed, the results of which are shown in Figure 3–1. The sensitivity of these two metrics to the continuity-background constraint weights is shown in Figure 3–1a-b. What is immediately evident in Figure 3–1a is the strong dependence of $V_{r,o}$ RMSE on λ_b, with little to no dependence on λ_c. Even with only a factor of two increase in λ_b over the radar observation constraint weight λ_o, the wind retrieval diverges substantially from the radar observations and converges towards the background wind field. As λ_b approaches 0.5, CSAPR-I7 $V_{r,o}$ RMSE approaches the specified upper limit of 1.5 m s^{-1}. This is important to note since proponents of 3D-VAR methods have reported the relative insensitivity of retrievals to minor changes (e.g., not orders of magnitude) in constraint weights [e.g., Gao et al., 1999; Potvin et al., 2012b]. However, in Figure 3–1b, λ_b has a decreased effect on the degree to which the wind retrieval satisfies mass continuity. As expected, this is primarily controlled

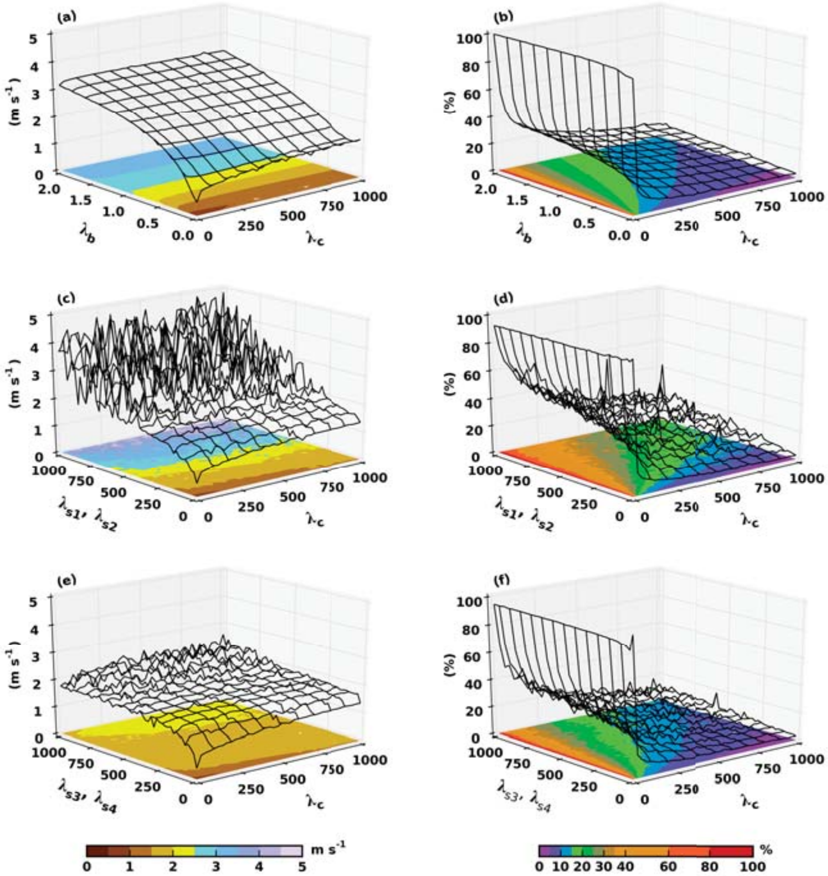

Figure 3–1: 3D-VAR constraint weight sensitivity analysis for two metrics: CSAPR-I7 radial velocity root mean squared error (left column) and relative mass continuity residual (right column). Sensitivity analysis is performed by perturbing (a-b) λ_c versus λ_b and (c-f) λ_c versus λ_{s1}-λ_{s4} constraint weights. Colours of the shaded region in each panel correspond to the projection of the surface plot. The nominal values of constraint weights not being tested in a given panel are set to those quoted in previous OSSE studies (see Table 3–1).

by λ_c, not only within the continuity-background parameter space but also in the continuity-smoothness parameter space shown in Figure 3–1c-f. The relative mass continuity residual α is particularly sensitive to λ_c when $\lambda_c < 250$. Outside of this range α is generally more stable with respect to λ_c and the relative mass continuity residual is typically below 20%. However, as seen in the right column of Figure 3–1, in order to obtain $\alpha \leq 5\%$, the mass continuity constraint λ_c must generally be 500 or larger.

Unlike the continuity-background sensitivity analyses, both metrics appear highly unstable in certain regions of the continuity-smoothness parameter spaces investigated in Figure 3–1c-f. For λ_{s1} and λ_{s2}, which control the degree of smoothing of the horizontal wind field in equation (3.7), CSAPR-I7 $V_{r,o}$ RMSE becomes unstable as these two weights approach values of 400 and larger. A similar phenomenon occurs for the relative mass continuity residual in Figure 3–1d. These highly unstable regions of the parameter space are likely the result of nonlinear effects introduced by the squared second order partial derivatives defined in J_s and should be avoided altogether. For values of λ_{s1} and λ_{s2} below approximately 100, CSAPR-I7 $V_{r,o}$ RMSE is within the 1.5 m s^{-1} threshold and relatively stable. However, the parameter space in which this holds true gradually decreases in size as λ_c increases towards 1000. Mass continuity is also adequately satisfied for $\lambda_{s1} = \lambda_{s2} < 100$ and $\lambda_c > 250$, with α typically below 10%. Results for λ_{s3} and λ_{s4} are similar to those of λ_{s1} and λ_{s2} except for one aspect. Since λ_{s3} and λ_{s4} control the degree of smoothing of the vertical wind component in J_s, these two constraint weights have little influence on the radar observations $V_{r,o}$ since the vertical wind

Table 3–1: Summary of 3D-VAR constraint weight ranges (parameter space) derived from sensitivity analyses. Study column indicates the constraint weight values used in this study. Nominal column reflects those from previous OSSE studies.

Constraint Weight	Range	Study	Nominal
λ_o	–	1 (max)	1
λ_c	(250, 1000)	500	–
λ_b	(0, 0.5)	0.01	0.01
λ_p	–	1000	–
λ_{s1}, λ_{s2}	(0, 100)	1, 1	1, 1
λ_{s3}, λ_{s4}	(0, 100)	1, 0.1	1, 0.1

component is generally not well sampled by scanning radars. This manifests itself in Figure 3–1e, which shows CSAPR-I7 $V_{r,o}$ RMSE to have much less dependence on λ_{s3} and λ_{s4} compared to λ_{s1} and λ_{s2}. A summary of the findings from these sensitivity analyses is recorded in Table 3–1. Recall that λ_o and λ_p were previously defined in Section 3.1 but are reiterated here for convenience.

Each sensitivity analysis in Figure 3–1 contains over 2000 individual wind retrievals, each of which was concurrently saved. Therefore, the spread of the wind field solution, in particular the vertical velocity solution spread, can be computed from these thousands of realizations, allowing us to address point (ii) above. It was found that within range of constraint weights defined in Table 3–1, the vertical velocity solution spread is quite narrow at 1.5 m s^{-1}. This also provides a form of uncertainty estimation for the 3D-VAR method used in this study. It follows that we expect the 3D-VAR vertical velocity retrievals to be relatively stable over a large range of constraint weights with uncertainties in vertical air motion on the order of 1-2 m s^{-1}.

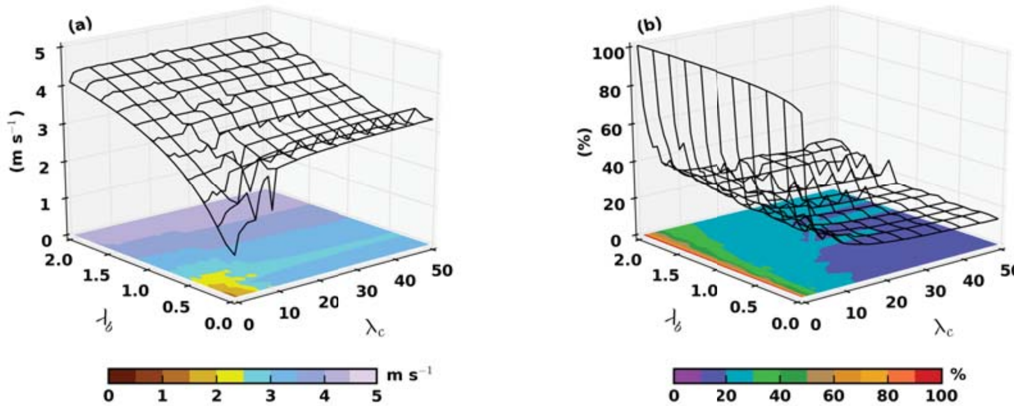

Figure 3–2: Traditional bottom-up method constraint weight sensitivity analysis for (a) CSAPR-I7 radial velocity root mean square error and (b) relative mass continuity residual. Sensitivity analysis is performed by perturbing λ_c-λ_b constraint weights. Colours of the shaded region in each panel correspond to the projection of the surface plot. The nominal values of constraint weights not being tested in a given panel are set to those quoted in previous OSSE studies (see Table 3–1).

A similar sensitivity analysis was done for a traditional, bottom-up method, the results of which are shown in Figure 3–2. Similar to the 3D-VAR results in Figure 3–1a, CSAPR-I7 $V_{r,o}$ RMSE is highly dependent on λ_b and less so on λ_c, however for $\lambda_c > 5$ there is a sharp increase in $V_{r,o}$ RMSE up to approximately 3 m s^{-1}, well outside the 1.5 m s^{-1} error limit. In fact, the parameter space in which $V_{r,o}$ RMSE is below 1.5 m s^{-1} is very small, and when looked at together with the relative mass continuity residual α, no continuity-background parameter space exists in which both metrics are reasonably satisfied. It is worth noting that as the influence mass continuity has on the wind retrieval is increased through increasing

λ_c, α appears to asymptote towards a value between 10% and 15%. This indicates that even in the parameter space where radar observations are effectively ignored (e.g., $V_{r,o}$ RMSE larger than 3 m s^{-1}), traditional bottom-up methods still have difficulty properly satisfying mass continuity. Results were also poor for the continuity-smoothness sensitivity analysis, in particular more unstable, and therefore they are not shown. As a result, traditional bottom-up wind retrievals shown in this study adopt the constraint weights shown in Table 3–1 except for λ_c, which was set to 1 in accordance with Collis et al. [2013]. Therefore, we do not expect traditional bottom-up wind retrievals to necessarily satisfy mass continuity but radar $V_{r,o}$ observations should be reasonably satisfied.

CHAPTER 4
RESULTS

Wind fields retrieved from scanning Doppler radars, with an emphasis on the vertical air motion, have not faced critical evaluation against independent observational datasets. Recently Collis et al. [2013] compared traditional dual-Doppler wind retrievals to corresponding dual-frequency wind profiler retrievals. The wind profiler location was along the dual-Doppler radar baseline, thus only an indirect statistical comparison was possible. Despite the suboptimal placement of the wind profiler, Collis et al. [2013] reported root mean square errors between the two vertical air motion retrievals on the order of 2 m s^{-1} for a dataset covering three characteristic events. Here, we will present results of vertical air motion retrievals from two distinct methods: using a radar wind profiler (UAZR) and a network of scanning Doppler radars. Contrary to the Collis et al. [2013] study, here the wind profilers were optimally placed away from radar baselines and in locations conducive for direct comparisons. Thus, we attempt to provide retrieval comparisons between these two methods in both time and space.

4.1 Collocated profiler matching criteria

It is important to note that several factors can contribute to the observed differences in the retrievals, including radar temporal sampling offsets, improper spatial alignment of illuminated radar volumes, beam broadening effects, as well as errors associated with possible radar miscalibration. The 6 second resampled temporal resolution of the UAZR (see Table 2–3) is considerably higher than that of the ARM scanning radar network, which samples similar volumes every 6-7 minutes (see Table 2–2). Furthermore the native 120 m range resolution of the UAZR is higher than the discrete height (elevation) sampling of the scanning radars, especially for higher elevation scans where consecutive elevations can be separated by more than 3 deg. Beam width and beam broadening effects must also be taken into account. Therefore a two-dimensional time-height median filter is first applied to all UAZR data in order to remove high frequency time-dependent phenomena and small-scale vertical structures unresolvable by the scanning radars. The time-height filter has a kernel that covers 61 profiles (6 minutes) in time and 7 range gates (840 m) in height.

At this point into the analysis the two datasets consist of the three-dimensional, regularly spaced (250 m resolution) scanning radar observations and retrievals, and the filtered time-height observations and retrievals from the radar wind profilers. Using the time record and the fixed location of the UAZRs, the closest scanning radar analysis grid column in space and time is identified. Surrounding each identified grid column we define a radius of influence R_s set to 750 m, which at 250 m resolution corresponds to 37 grid points at each height. The radius of influence R_s is designed to account for the spatiotemporal differences in the sampling strategies between the two datasets as well as the advection of the cloud system. Furthermore, at each grid height, the median value within R_s is used as the best estimate, and the range of values within R_s are used to estimate the variability (e.g., spatial uncertainty) of the scanning radar network observations and retrievals. Similarly, at each UAZR range (height) gate, the median value within the time window of the corresponding scanning radar data (herein valid time) is used as the best estimate for the UAZR, and the range of UAZR values within the valid time is used to characterize its variability. Several common error statistics are used to compare the two datasets: mean bias error (MBE), mean absolute error (MAE), root mean square error (RMSE), Spearman's rank correlation (ρ), and the Pearson product-moment correlation (r). Difference statistics are computed subtracting UAZR from scanning radar, so a negative bias implies the scanning radar dataset underestimated the UAZR dataset.

4.2 Radar reflectivity evaluation

The aforementioned matching criteria for comparing the two datasets is evaluated by comparing radar reflectivity Z_H measurements observed by UAZR-C1 with those from CSAPR-I7. These measurements are direct and the two radars are calibrated. The UAZR receiver is known to saturate below 1 km range in heavy precipitation (e.g., $\sim$ 45 dBZ at 1 km range), therefore comparisons are performed above this level. Below the melting layer, the two Z_H time series are moderately correlated, with ρ and r typically above 0.8 and 0.6, respectively, and MAE below 3 dBZ. Table 4–1 provides a summary of each comparative statistic at three characteristic heights for all events. The characteristic heights represent those below the melting layer (2 km) and above the melting layer (6-8 km). We note that the comparisons typically deteriorate within the melting layer (2.5-3.5 km AGL) due to additional wavelength-dependent scattering factors.

Table 4–1: Radar reflectivity comparisons between CSAPR-I7 and UAZR-C1 at three characteristic heights for all events. Error statistics have units of dBZ.

Event	Height (km AGL)	Sample Size	MBE	MAE	RMSE	ρ	r
25 Apr 2011							
	2	28	-1.00	2.22	3.79	0.95	0.80
	6	23	-1.62	2.73	3.51	0.93	0.64
	8	24	-1.09	2.50	3.81	0.92	0.67
	All	864	-0.94	2.97	3.96	0.94	0.55
11 May 2011							
	2	70	-2.11	2.45	3.57	0.86	0.47
	6	85	-2.04	2.23	2.98	0.62	0.44
	8	69	-0.41	1.62	2.11	0.87	0.38
	All	2462	-1.16	1.98	2.79	0.92	0.40
20 May 2011							
	2	52	-2.11	2.33	3.24	0.97	0.77
	6	68	-1.90	2.28	3.79	0.79	0.76
	8	54	-1.29	1.79	3.60	0.85	0.70
	All	1983	-1.66	2.32	3.71	0.90	0.62
23 May 2011							
	2	6	-1.10	3.29	3.68	0.73	0.53
	6	19	-3.86	4.02	4.83	0.86	0.59
	8	11	-0.94	1.97	2.34	0.73	0.39
	All	398	-1.75	3.18	4.03	0.82	0.34
24 May 2011							
	2	6	-0.98	2.45	3.03	0.66	0.48
	6	16	-1.51	3.41	4.85	0.90	0.69
	8	29	-1.31	3.77	4.45	0.72	0.58
	All	557	-0.93	3.50	4.58	0.86	0.44

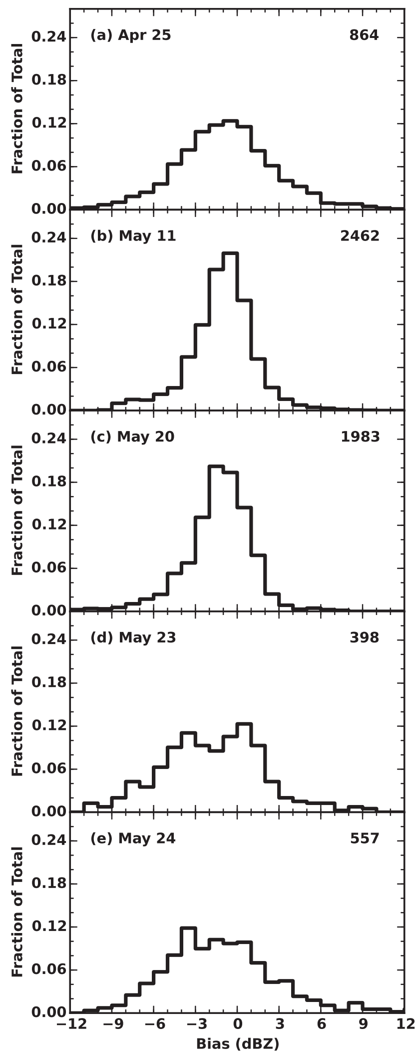

Figure 4–1: Histograms of radar reflectivity differences between CSAPR-I7 and UAZR-C1 for (a) 25 Apr 2011 (c) 20 May 2011 (d) 23 May 2011 and (e) 24 May 2011. Due to CSAPR-I7 not being operational on 11 May 2011, differences in (b) are between KVNX and UAZR-C1. Sample sizes are recorded for each event. Bin widths are 1 dB. Differences were computed subtracting radar wind profiler from scanning radar.

A summary of the Z_H biases between UAZR-C1 and CSAPR-I7 for each event is provided in Figure 4–1. Figure 4–1b indicates the biases in Z_H between KVNX and UAZR-C1 since CSAPR-I7 was not operational. The negative skewness and negative mean bias for each event is likely the result of the smoothing introduced while mapping the scanning radar data. The 23-24 May events were short lived over UAZR-C1 (see Table 2–1), therefore a limited amount of data was available for comparison and therefore the resulting distributions have a large spread. Nonetheless, these two events still have mean bias errors below -2 dBZ and moderate correlation coefficients (Table 4–1). The 11 and 20 May events, which were observed by UAZR-C1 for five hours or more and therefore have the largest sample sizes, both have narrow distributions with means around -1.5 dBZ. Considering the intrinsic differences and possible sources of error between scanning and profiling radar observations, we conclude that the methodology outlined for comparing the two datasets successful.

Figure 4–2 shows the direct Z_H time series of both CSAPR-I7 and UAZR-C1 at the three characteristic heights during 20 May 2011. The two datasets are visually highly correlated, with Table 4–1 indicating correlation coefficients typically above 0.8, MAE below 2.5 dBZ, and RMSE below 3.8 dBZ. This particular event contained the formation and subsequent passage of a squall line directly over CSAPR-I7 around 1040 UTC. Radome-induced attenuation effects on the measured CSAPR-I7 reflectivities can be seen in Figure 4–2 as the large Z_H difference between the two radars by 1030-1100 UTC. This highlights the need to incorporate observations from a longer-wavelength radar such as KVNX which is

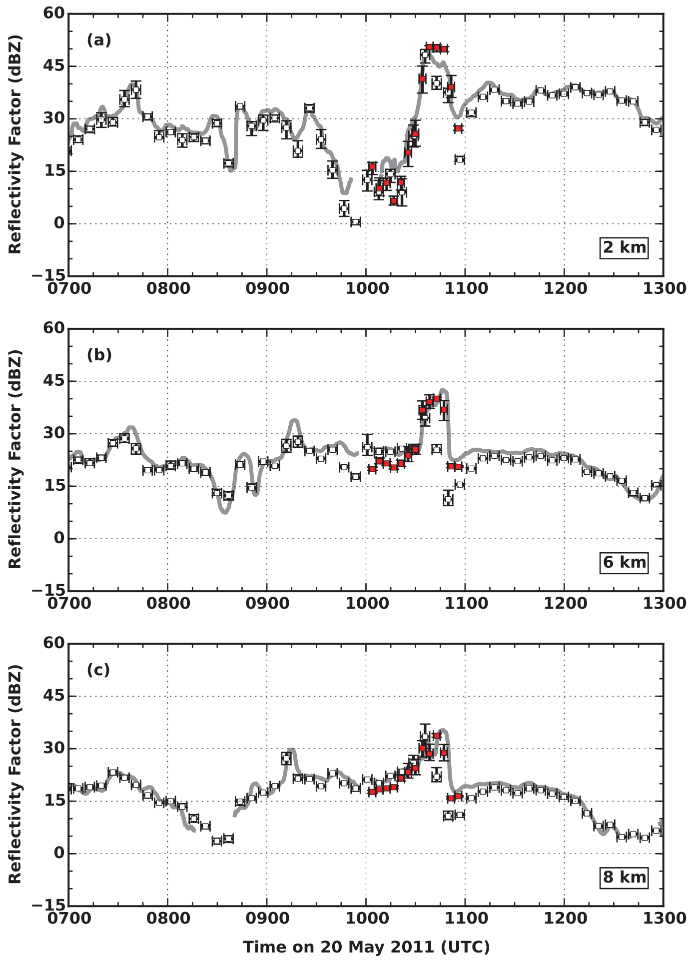

Figure 4–2: Radar reflectivity observations on 20 May 2011 at three characteristic heights (a) 2 km (b) 6 km and (c) 8 km AGL. Discrete white and red markers with error bars correspond to CSAPR-I7 and KVNX observations, respectively, with error bars indicating the full range of Z_H values in R_s and the scanning radar valid time. Continuous solid gray line corresponds to UAZR-C1 observations, which have been filtered using a 61 x 7 time-height median filter. KVNX observations are shown between 1000-1100 UTC, exclusively.

less susceptible to radome and path attenuation in heavy rain. To demonstrate this, KVNX Z_H is superimposed in Figure 4–2 exclusively between 1000-1100 UTC to show the improvement it offers in Z_H observations of the squall line.

Overall, the Z_H comparisons shown here indicate that these two distinct, independent datasets can be reasonably well-matched. Finally, the observed discrepancies between Z_H as indicated by both the MAE and RMSE values are arguably comparable to the limit one may be able to reliably calibrate radar systems using natural media under Oklahoma conditions [Ryzhkov et al., 2005; Giangrande and Ryzhkov, 2005].

4.3 Vertical velocity evaluation

The 25 April 2011 event was the first well-coordinated aircraft-ground precipitation mission during MC3E. Convective cells developed during the nighttime across northern parts of Oklahoma and along an elevated front, aided by mid to upper-level ascent associated with the passage of an upper-level trough. The convective cells were relatively shallow in depth. Figure 4–3a shows the time-height of vertical air motion retrievals and corresponding reflectivity from UAZR-C1. The closest available 3D-VAR retrieval and its reflectivity field are shown in Figure 4–3b-e. Note that the UAZR-C1 data is the original, unfiltered data. The 3D-VAR retrieval used scanning radar observations recorded between 0916-0924 UTC, spanning a total of 8 minutes. UAZR-C1 is located at the origin in Figure 4–3b-e. The most prominent feature in both retrievals is the elevated updraft with an apparent base extending slightly below 4 km AGL, a depth of 5-6 km, and an intensity greater than 8 m s^{-1}. The local cloud system advection was estimated to

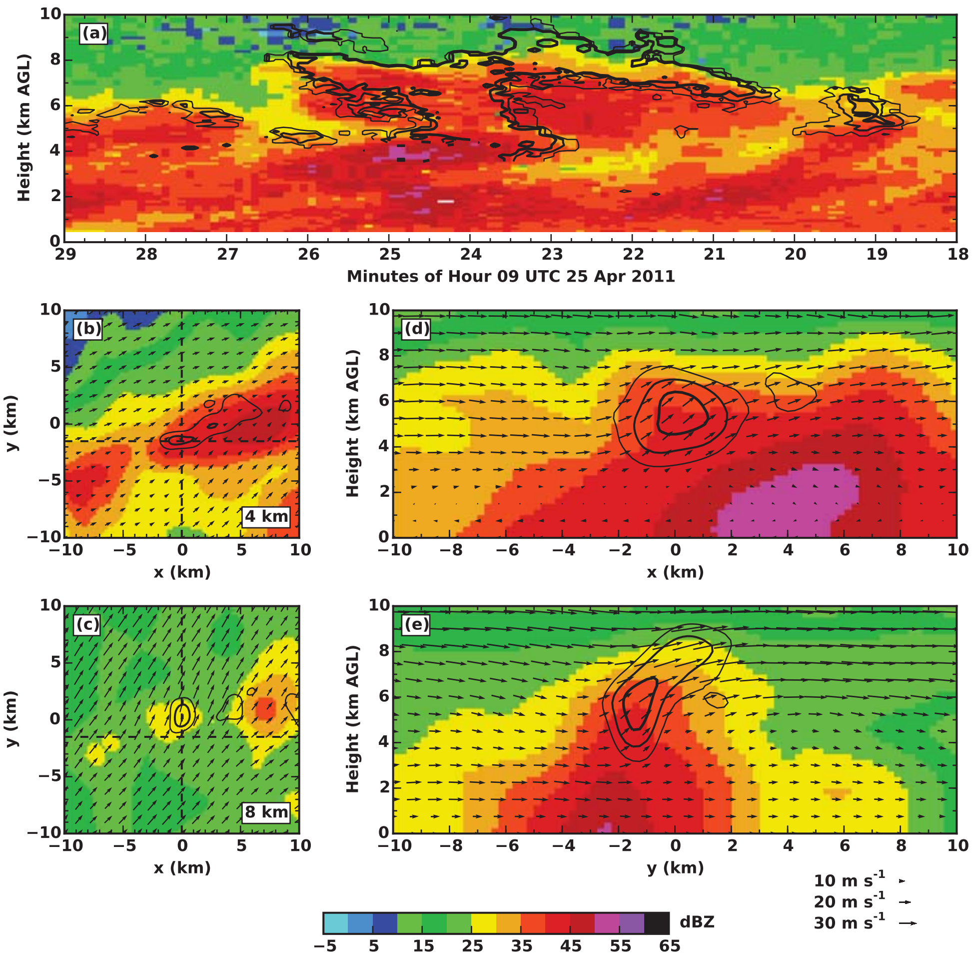

Figure 4–3: Two independent vertical air motion retrievals on 25 Apr 2011 from (a) 915-MHz radar wind profiler (UAZR-C1) and (b-e) 3D-VAR. Radar reflectivity background and vertical velocity contours of 4 (light), 6 (medium), and 8 (thick) m s^{-1} are shown in all panels. Wind vectors are shown in every 3D-VAR panel. The horizontal cross sections shown in (b-c) are at 4 and 8 km AGL, respectively, with dashed black lines indicating the corresponding vertical cross sections in (d-e). The 3D-VAR retrieval was derived from scanning radar observations recorded between 0916-0924 UTC. The origin in (b-e) corresponds to the location of UAZR-C1.

be 18 m s^{-1} by Giangrande et al. [2013a], with a north-northeast direction inferred by comparing successive CSAPR-I7 reflectivity displays. Therefore the time axis in Figure 4–3a was reversed to better represent what the updraft retrieved by UAZR-C1 would look like in the north-south vertical cross section in Figure 4–3e. The base of the updraft retrieved by UAZR-C1 is first seen at approximately 0923 UTC, which is near the end of the 3D-VAR valid time window. The base of the updraft in the 3D-VAR retrieval is approximately 2 km south of UAZR-C1, and with the prescribed cloud motion would pass over UAZR-C1 2 minutes later. This 2 minute (2 km) offset is consistent with the UAZR-C1 retrieval if we assume that the 3D-VAR retrieval is valid at 0921 UTC, which is within the valid time. We note that a precise reference time for the 3D-VAR retrieval does not exist, but the two independent vertical air motion retrievals are qualitatively consistent with one another in terms of the relative location of the main updraft, its base height and depth, and its overall intensity.

A more direct time-height comparison between these two methods for the same event covering 0900-1045 UTC is provided in Figure 4–4. In this case, the UAZR-C1 data has been filtered using the 61 x 7 time-height median filter. The elevated updraft seen in Figure 4–3 is easily identifiable in the 6 km and 8 km AGL panels between 0915-0930 UTC for both retrievals, with each showing the updraft strength to be stronger at 8 km rather than 6 km AGL. Visually the two retrievals are reasonably correlated at each height, with $r = 0.51$ and MAE less than 2 m s^{-1} at 6 km AGL (Table 4–2). The updraft retrieved by the 3D-VAR method as seen in Figure 4–3 that was offset by approximately 2 minutes

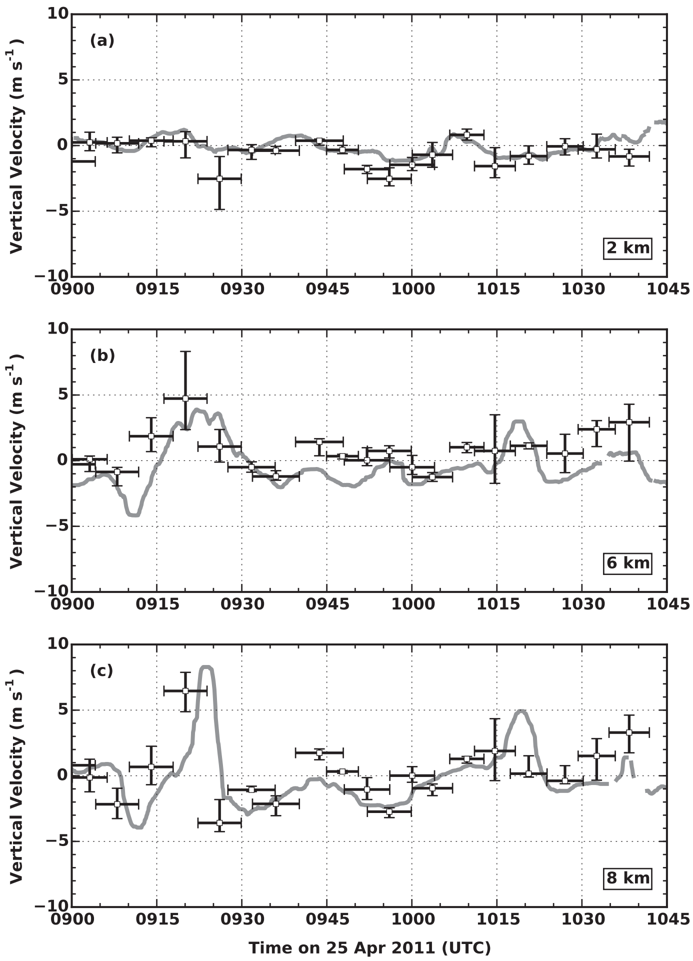

Figure 4–4: Vertical air motion time series on 25 Apr 2011 at three characteristic heights (a) 2 km (b) 6 km and (c) 8 km AGL. Discrete circular markers with error bars represent 3D-VAR retrievals, where error bars indicate the full range of w values in R_s and the 3D-VAR valid time. Continuous solid gray line represents UAZR-C1 retrievals, which have been filtered using a 61 x 7 time-height median filter.

(2 km) from the UAZR-C1 location is well-captured by the 3D-VAR error bars between 0915-0930 UTC in Figure 4–4b-c. Table 4–2 lists the remaining errors and correlations between the two methods for this event. At most characteristic heights vertical velocity bias is near 0.5 m s^{-1} and absolute error is less than 2 m s^{-1}. This is arguably negligible when considering the inherent differences between the two methods and the small percent error this would suggest between intense convective drafts (e.g., 10-20 m s^{-1}). The correlation coefficients are moderate at heights 6 km AGL and below (not all shown), with values of ρ and r between 0.4 and 0.6. At higher altitudes such as 8 km AGL, correlations are weaker and errors are larger, likely the result of the elevated nature of this event and thus the stronger dynamics aloft. That said, the vertical air motion time series at 8 km AGL still appears to show some skill between the two methods, with a bias less than 0.5 m s^{-1} and 3D-VAR error bars indicating a better correlation than is otherwise shown at this height in Table 4–2.

The 20 May 2011 event was the longest lived propagating MCS sampled by the scanning radar network.. UAZR-C1 observed leading stratiform precipitation and shallow convection throughout 0600-1000 UTC, followed by deep convection between 1000-1100 UTC which ultimately produced a large region of trailing stratiform precipitation that existed over UAZR-C1 for another 4-5 hours. The most interesting feature of this event from a wind retrieval standpoint was the development of a squall line, passing over UAZR-C1 around 1040 UTC. Similar to Figure 4–4, the time-height comparisons between UAZR-C1 and 3D-VAR wind retrievals for this event are shown in Figure 4–5, covering the 6 hours between

Table 4–2: Vertical air motion comparisons between 3D-VAR and UAZR-C1 at three characteristic heights for all events. Error statistics have units of m s^{-1}.

Event	Height (km AGL)	Sample Size	MBE	MAE	RMSE	ρ	r
25 Apr 2011							
	2	20	-0.46	0.65	0.92	0.54	0.53
	6	20	1.18	1.58	1.86	0.43	0.51
	8	20	0.43	2.17	3.09	0.23	-0.03
	All	676	0.50	1.63	2.22	0.14	0.11
11 May 2011							
	2	27	0.02	0.79	1.05	0.34	0.35
	6	27	0.66	0.93	1.08	0.51	0.55
	8	27	0.23	0.61	0.74	0.68	0.63
	All	897	0.45	0.87	1.07	0.48	0.48
20 May 2011							
	2	55	0.38	0.99	1.24	0.22	0.69
	6	58	0.35	0.86	1.22	0.44	0.61
	8	51	0.14	0.94	1.49	0.38	0.15
	All	1871	0.29	0.92	1.27	0.32	0.50
23 May 2011							
	2	6	0.54	1.01	1.45	0.33	0.33
	6	19	0.42	0.99	2.31	0.32	0.41
	8	11	0.50	1.88	1.89	0.21	0.40
	All	398	0.52	1.74	2.11	0.29	0.40
24 May 2011							
	2	6	0.36	0.98	1.21	0.34	0.31
	6	16	0.39	1.32	1.75	0.51	0.29
	8	29	0.49	1.87	2.02	0.42	0.35
	All	557	0.50	1.41	2.01	0.49	0.47

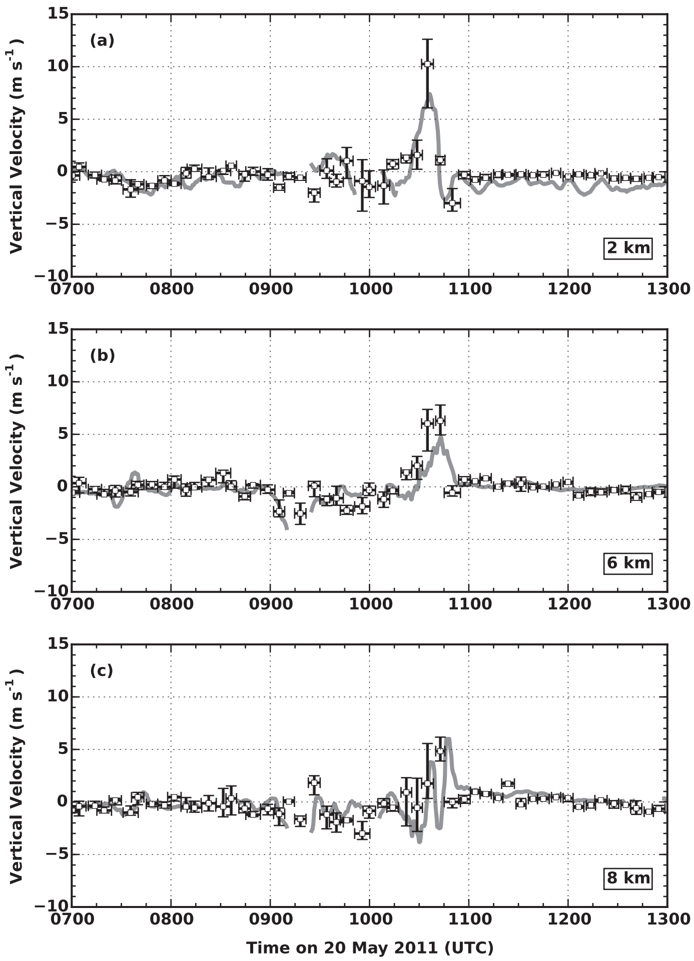

Figure 4–5: Vertical air motion time series on 20 May 2011 at three characteristic heights (a) 2 km (b) 6 km and (c) 8 km AGL. Discrete circular markers with error bars represent 3D-VAR retrievals, with error bars indicating the full range of w values in R_s and the 3D-VAR valid time. Continuous solid gray line represents UAZR-C1 retrievals, which have been filtering using a 61 x 7 time-height median filter.

0700-1300 UTC. Strong upwards motion associated with the squall line surface convergence zone is immediately visible at the 2 km AGL time series in Figure 4–5a for both methods. The 3D-VAR vertical velocities near this time at 2 km AGL reach upwards of 13 m s^{-1}, similar to the instantaneous, unfiltered values retrieved by UAZR-C1 (not shown). The large range of vertical velocities in R_s (e.g., $\sim$ 8 m s^{-1} at 2 km AGL) between 1015-1045 UTC are an indication of the strong dynamics associated with the squall line. Overall there is good agreement between the two methods surrounding the squall line as well as throughout the rest of the 6 hour period. Vertical velocity correlations as high as 0.7-0.8 were found at select heights between 2 km and 8 km AGL (not shown), with the entire event producing a moderate correlation of r = 0.5 (see Table 4–2). Vertical velocity errors were also relatively small, with biases approaching 0.3 m s^{-1}, absolute errors no larger than 1 m s^{-1}, and root mean square errors below 1.5 m s^{-1}.

Results from the 11 May 2011 event are unique in that CSAPR-I7 was not operational and therefore 3D-VAR wind retrievals were derived from one less source of information compared to the other events. The effect this has on the quality of 3D-VAR wind retrievals is important to quantify. Table 4–2 and Figure 4–6 provide insights into the overall net effects a missing radar had on the retrievals in terms of agreement with UAZR-C1. Here we focus on the differences between 11 May and 20 May, which had the largest time-height sample sizes. Bias error distributions shown in Figure 4–6 are similar for both events, with 11 May producing a slightly larger positive mean bias. In particular, the percent change in mean bias error between the two events is approximately 55% (0.29 m s^{-1} for

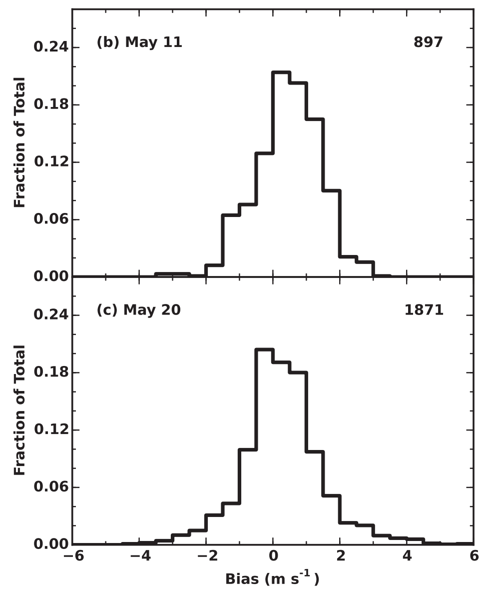

Figure 4–6: Histograms of vertical velocity differences between 3D-VAR and UAZR-C1 retrievals for (a) 11 May 2011 and (b) 20 May 2011. Sample sizes are recorded for each event. Bin widths are 0.5 m s^{-1}. Differences were computed subtracting UAZR-C1 from 3D-VAR.

20 May versus 0.45 m s^{-1} for 11 May), however both are less than 0.5 m s^{-1} and thus arguably insignificant. Only a 6% change in mean absolute error was found between the two events. Correlations are moderate for both events, with 11 May having a slightly larger ρ correlation but slightly smaller r correlation. Overall, more than one event or dataset is required to more accurately quantify these differences, however, these results show that performing 3D-VAR wind retrievals with an additional radar likely has the most significant impact on reducing vertical velocity bias error.

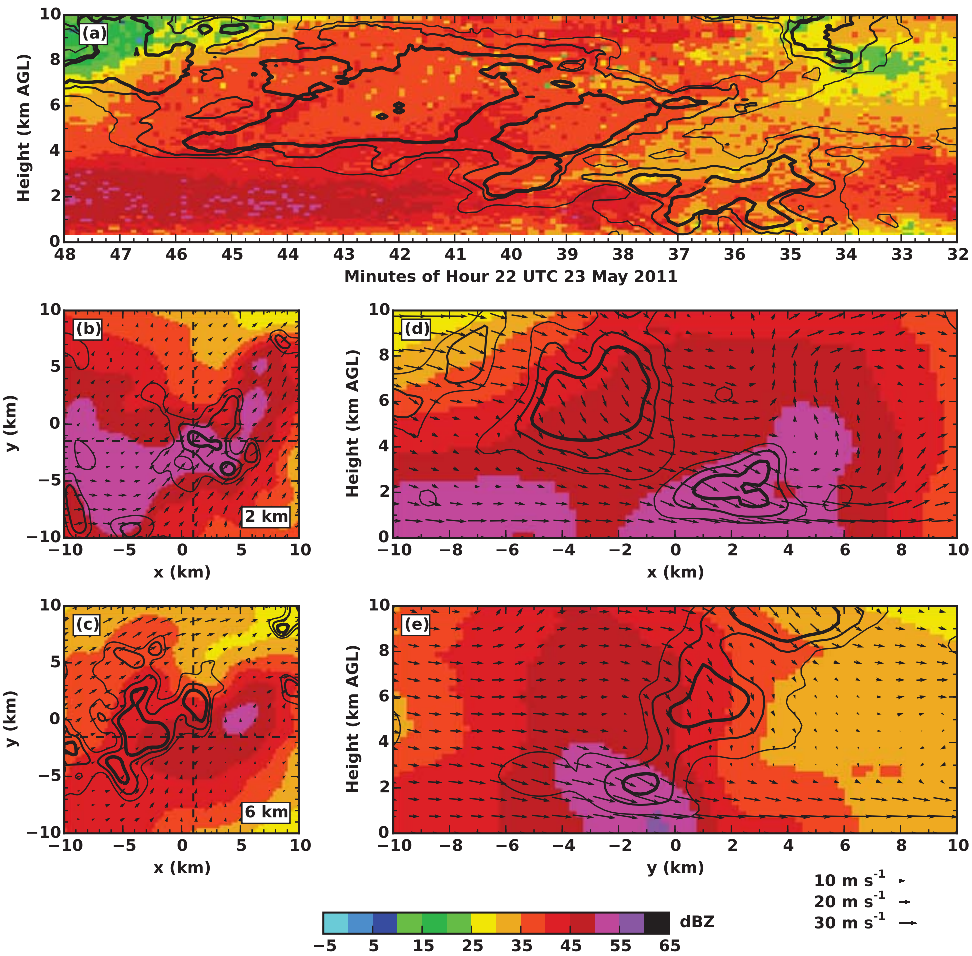

Figure 4–7: Two independent vertical air motion retrievals on 23 May 2011 from (a) 915-MHz radar wind profiler (UAZR-I9) and (b-e) 3D-VAR. Radar reflectivity background and vertical velocity contours of -4 (light), -6 (medium), and -8 (thick) m s^{-1} are shown in all panels. Wind vectors are shown in all 3D-VAR panels. Horizontal cross sections shown in (b-c) are at 2 and 6 km AGL, respectively, with dashed black lines indicating the corresponding vertical cross sections in (d-e). The 3D-VAR retrieval was derived from scanning radar observations recorded between 2236-2243 UTC. The origin in (b-e) corresponds to the location of UAZR-I9.

The 23 May 2011 event was part of an active sequence of severe convective outbreak days over the central plains, including within the multi-Doppler analysis domain. A surface low pressure system located over the Texas panhandle and the associated surface boundaries were focal points for late afternoon convection. The environmental forcing coupled with strong daytime heating led to significant instability in addition to deep layer shear consistent with the eventual development of strong, discrete supercells. Convection captured within the analysis domain developed ahead of a surface dry line in western Oklahoma, coinciding with the passage of a shortwave trough. Supercells propagated eastward into the analysis domain by 2100 UTC, with UAZR-I9 observing intense, deep convection between 2200-2300 UTC. Near 2235 UTC UAZR-I9 retrieved strong downdrafts reaching the surface with magnitudes larger than 8 m s^{-1}, with the core of the downdrafts increasing in height in the 8-10 minutes that followed. These results are shown in Figure 4–7a. The closest available 3D-VAR retrieval, valid between 2236-2243 UTC, is shown in Figure 4–7b-e. Due to the east-northeast propagation of the local cloud system, the time axis in Figure 4–7a was reversed to better reflect the east-west cross section through the 3D-VAR retrieval in Figure 4–7d. Cloud advection speed was estimated by Giangrande et al. [2013a] to be 17 m s^{-1}, indicating that the total downdraft feature retrieved by UAZR-I9 between roughly 2235-2245 UTC (10 minutes) covered approximately 10 km in length. This length is consistent with the east-west length of the total downdraft feature retrieved by the 3D-VAR method in Figure 4–7d, which covers the zonal length roughly between x = -6 km and x = 4 km. Furthermore, the behaviour of the retrieved

3D-VAR downdraft is consistent with that of UAZR-I9, namely a surface bound downdraft which appears to elevate as time (displacement) increases.

4.4 3D-VAR versus traditional wind retrievals

Some of the added benefits of 3D-VAR over traditional bottom-up wind retrievals were presented in Section 3.2 through an extensive sensitivity analysis. It was shown that there was a large parameter space in which the 3D-VAR method was able to simultaneously satisfy radar observations and mass continuity, with the retrieved vertical velocity relatively stable over this space. The same could not be said for the traditional bottom-up approach, which never adequately satisfied mass continuity (e.g., α was never less than 10%) and radar observations were, for the most part, difficult to adequately satisfy. Here we investigate what role this has on the actual wind fields retrieved by both these methods. This is accomplished by selecting the squall line event on 20 May 2011, which had substantial surface wind convergence ahead of the line that was well-sampled by the scanning radar network. Strong wind convergence at or near the surface was indirectly observed around 1040 UTC by UAZR-C1 as strong upwards motion lasting close to 5 minutes (see Figure 4–5a for an indication). A bottom-up integration method is ideal for surface-driven events since the horizontal wind divergence profile should be well defined, particularly near the lower boundary.

Figure 4–8 presents wind retrievals from these two methods within the 20 km x 20 km surrounding UAZR-C1. Both methods retrieve similar wind convergence pattern and upwards motion at 1 km AGL, with the traditional bottom-up method retrieving a slightly stronger convergence line near the surface

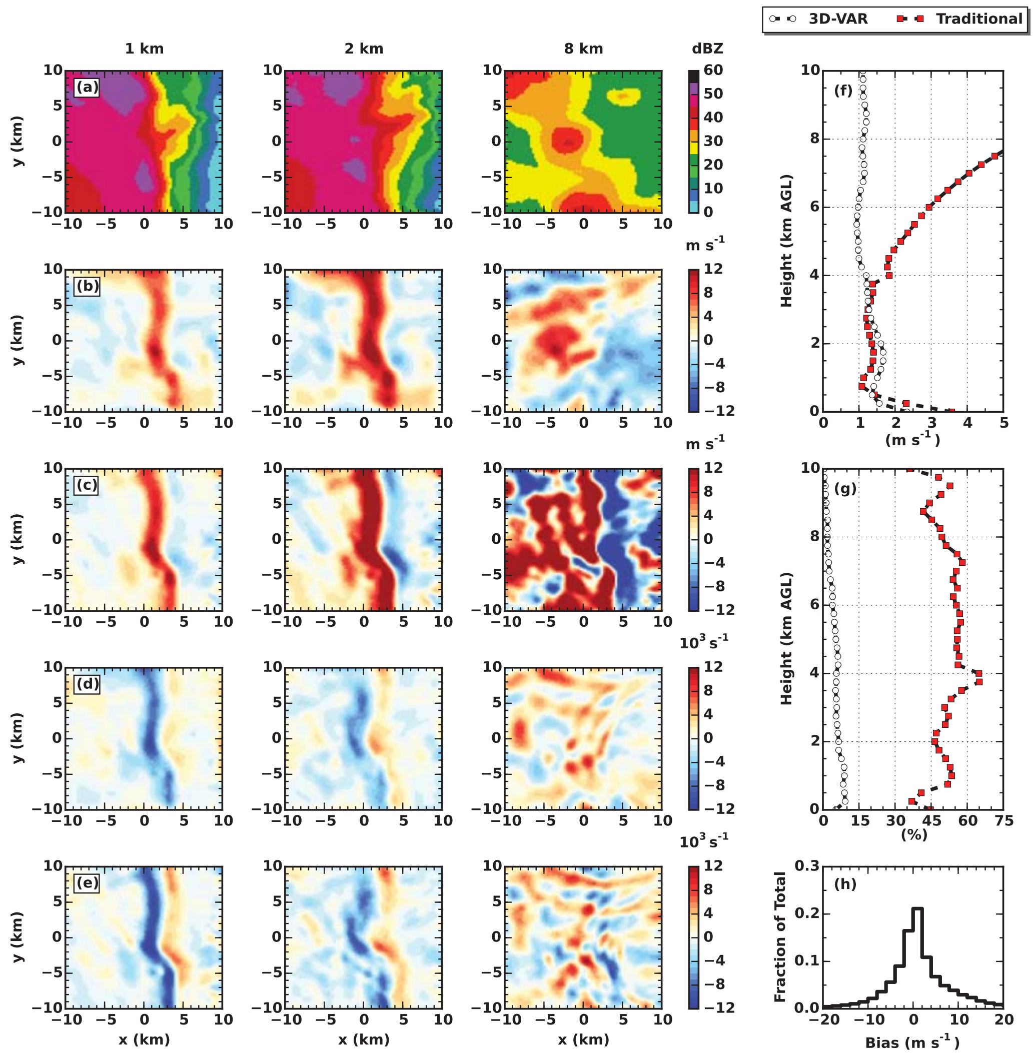

Figure 4–8: Comparison of squall line wind retrieval between 3D-VAR and a traditional bottom-up method on 20 May 2011, showing (a) radar reflectivity (b-c) 3D-VAR and traditional vertical air motion, respectively (d-e) 3D-VAR and traditional horizontal wind divergence, respectively (f) CSAPR-I7 $V_{r,o}$ RMSE (g) relative mass continuity residual and (h) vertical air motion difference (3D-VAR minus traditional; 2 m s^{-1} bin width). Select heights for (a-e) are 1 km, 2 km, and 8 km AGL. Origin in (a-e) corresponds to location of UAZR-C1.

and therefore enhanced upwards air motion near the surface. Both methods also satisfy the radar observations to similar degrees below 2 km AGL, as shown in Figure 4–8f. However, as expected, there is a large discrepancy between the two methods (e.g., $\sim$ 60% at 4 km AGL) when it comes to satisfying anelastic mass continuity. At each analysis height in Figure 4–8g, the 3D-VAR method is adequately satisfying mass continuity, with $\alpha < 10\%$ at each height and $\alpha = 5\%$ over the entire domain. For the traditional bottom-up method, α never gets below 30% at any given height, and over the entire domain $\alpha = 52\%$. The accumulation of vertical velocity errors in the bottom-up solution as a result of inadequately satisfying mass continuity becomes more pronounced with increasing height, and at 8 km AGL, there is no longer similar spatial patterns or intensities in the vertical velocity field between the 3D-VAR and traditional bottom-up method. This accumulation of errors with height is most evident in Figure 4–8f. For the traditional bottom-up method, CSAPR-I7 $V_{r,o}$ RMSE quickly increases past 2 m s^{-1} for heights above 5 km AGL whereas the 3D-VAR method is able to satisfy CSAPR-I7 $V_{r,o}$ observations at almost all analysis heights. As a result, the large spread in vertical air motion bias between the two methods in Figure 4–8h comes from analysis heights above 5 km AGL. Over the entire analysis domain, vertical velocity MBE, MAE, and RMSE are all significant at 1.3 m s^{-1}, 5.8 m s^{-1}, and 7.7 m s^{-1}, respectively. Conditionally sampling the two retrievals below 5 km AGL, the MBE, MAE, and RMSE decrease substantially to 0.5 m s^{-1} (38%), 2.6 m s^{-1} (45%), and 3.9 m s^{-1} (51%), respectively. Nonetheless, this still represents large differences in the wind fields retrieved by each method.

Finally, the physical explanation for why the vertical velocity of the traditional bottom-up solution appears to *run away* with increasing height is the following. First, as equation (3.5) shows, no wind divergence information above the integration level k is used as input to compute w_c. This, coupled with decreasing air density with height, leads to a situation in which the momentum of an air parcel becomes unconstrained and the parcel is free to accelerate away from its original location.

CHAPTER 5
SUMMARY AND DISCUSSION

This study describes the first operational use of the ARM SGP advanced heterogeneous scanning radar network during MC3E, a joint field campaign between the DOE ARM program and NASA GPM mission GV program. This field campaign included the acquisition of over 40 days of data, collected from several remote and in situ sensors. The five most prominent convective events observed during MC3E were studied here. The details about each instrument used have been discussed, most notably the ARM X- and C-band scanning radars and collocated radar wind profilers. Advanced algorithms were employed for the scanning radars to properly address common radar data artifacts including ground clutter identification and removal, Doppler velocity dealiasing, and attenuation correction in rain at C-band. Radar echo classification was done using a naive Bayes classifier, designed and calibrated for each ARM scanning radar system. This included manually identifying hundreds of radar volumes throughout the MC3E that were primarily characterized by ground clutter or hydrometeors in order to properly calibrate the Bayes classifier for each radar. The classification results were very promising, and there are plans to incorporate these methods into an ARM value added product (VAP), providing quality controlled raw data to the greater ARM community seeking to use scanning radar data. With the inclusion of the NEXRAD WSR-88D radar network, specifically KVNX, this study also marks the first time X-, C-, and S-band scanning radars have been used to pseudo simultaneously view the atmosphere from multiple different angles and retrieve the wind field over a large domain.

A detailed background on multi-Doppler wind retrieval methods was provided in Section 3.1. This included the more recent developments in 3D-VAR methods as well as how these methods relate to traditional multi-Doppler techniques. A novel radar observation weight was introduced in equation (3.3) in order to address the varying degrees of spatial coverage between the ARM and NEXRAD scanning radars. A practical sensitivity analysis designed to produce robust wind retrievals when no truth field is available was also introduced in Section 3.2. The main approach behind this analysis was to define the constraint weight parameter space in which radar observations and anelastic mass continuity were simultaneously adequately satisfied. First, the identification of a range of radar Doppler velocity observation errors is required, which should include the errors associated with measurement as well as the mapping from discrete sampling locations to a uniform grid. If the root mean squared error between the wind retrieval V_r and the radar $V_{r,o}$ observations was larger than the estimated $V_{r,o}$ uncertainty, than the wind retrieval was considered suspect. For this study, a [0.5, 1.5] m s^{-1} error range for $V_{r,o}$ was specified. The degree to which anelastic mass continuity was satisfied was computed using equation (3.9), which we refer to as the relative mass continuity residual. The closer α is to 0%, the closer anelastic mass continuity is to being perfectly satisfied, however it is still an underlying assumption and therefore anelastic mass continuity should not be perfectly satisfied. Therefore, we specified a range of [1%, 10%] for the relative mass continuity residual. Extensive sensitivity analyses were then done in order to determine the parameter space of multiple constraint weights which satisfied these two conditions, the results of which are summarized in Table 3–1. For the 3D-VAR method, a large parameter space existed in which radar observations and mass continuity were both adequately satisfied. Within this parameter space, it was found that the vertical velocity solution spread derived from the individual realizations of the wind field was relatively narrow, on the order of 1-2 m s^{-1}, indicating that 3D-VAR retrievals of vertical velocity are quite stable and their uncertainties relatively small over a large range of constraint weights. A similar analysis was done for a traditional bottom-up method, the results of which were poor compared to the 3D-VAR method. Most importantly, the traditional bottom-up method was unable to simultaneously satisfy radar observations and anelastic mass continuity. Furthermore, the parameter space in which radar observations were reasonably satisfied was relatively small, indicating that radar observations are difficult to satisfy when using a traditional bottom-up approach. Finally, in the parameter space where radar observations were effectively ignored (e.g., $V_{r,o}$ RMSE greater than 3 m s^{-1}), the relative mass continuity residual α was found to asymptote to a value between 10% and 15%, indicating that traditional bottom-up methods also have difficulty satisfying mass continuity.

Results were broken up into three main sections. The first evaluated how well collocated column measurements of radar reflectivity from radar wind profilers could be matched with those from scanning radars, the results of which were generally successful. Time-height comparisons showed good visual agreement between the Z_H measurements, which was reinforced by correlations greater than 0.8 at most heights, biases close to -1.5 dBZ, and absolute errors typically less than 3 dBZ. These errors are arguably at the limits in which weather radars may be reliably calibrated with natural media. Following reflectivity evaluation, a similar evaluation was done on the retrieved vertical air motion between the UAZRs and the 3D-VAR method described in Section 3.1. The results from this were encouraging. The spatial and temporal characteristics of the 3D-VAR vertical velocity retrievals were generally in good agreement with those from the profiling radars. Prominent updraft and downdraft features retrieved by the UAZRs were repeatedly observed in the 3D-VAR dataset. Direct time-height comparisons showed reasonable agreement for most events analyzed, with moderate correlations on the order of 0.5. An evaluation of the vertical velocity errors between the two methods further justify a level of optimism. Bias errors were typically less than 0.5 m s^{-1}, absolute errors within 1 m s^{-1}, and root mean square errors generally less than 1.5 m s^{-1}. In the context of deep convective drafts, where velocities can exceed 15 m s^{-1}, these errors are arguably negligible. A final evaluation of the wind field surrounding the 20 May 2011 squall line was done in Section 4.4. Here we investigated the underlying differences between the 3D-VAR and traditional bottom-up retrievals. Below approximately 5 km AGL, the two methods retrieved similar vertical velocity spatial patterns, including a large region of upwards motion associated with the surface wind convergence zone. However, the magnitudes of the vertical velocities between the two methods were considerably different, with MAE and RMSE on the order of 3 m s^{-1} and 4 m s^{-1}, respectively. Upon further investigation, these large differences were caused by the traditional bottom-up method inadequately satisfying mass continuity. In particular, the relative mass continuity residual over the entire analysis domain was 52% for the traditional method compared to 5% for the 3D-VAR retrieval. Additionally, radar $V_{r,o}$ RMSE quickly diverged past 2 m s^{-1} for heights above 5 km AGL for the traditional method, further indicating suspect results. Overall, the traditional bottom-up wind retrieval was inferior to its 3D-VAR counterpart.

Further examination is needed to assess the quality of 3D-VAR wind retrievals in terms of radar network size and number of scanning radar inputs, which was only briefly investigated in this study. For example, it would be beneficial to properly characterize the expected deterioration in vertical air motion retrievals when one or more radars are nonoperational in the network, a common scenario for real scanning radar networks. Additionally, the value of single-Doppler 3D-VAR wind retrievals, with an emphasis on vertical velocity, to those from two or more radars could be investigated. If vertical air motion retrievals from a single Doppler radar are shown to possess a certain level of skill, this could have immediate effects on operational weather radars used for aviation and other hazard forecasting purposes.

While only five events were available for proper study out of the whole of MC3E, with not all profiling radars available or adequately sampling these five events, the ARM SGP site promises to provide a unique dataset moving forward due to its continuous operation. Plans for a second C-band radar to be placed due south of the SGP Central Facility are currently in the works, which would provide an additional constraint for convective air motion retrievals. With this in mind, we have the ability to create a continuous, high quality dataset of continental convective air motions over a large domain derived from multiple scanning radar observations. This dataset would provide, at minimum, an additional observational constraint for improving current convective parameterizations used in CRMs and ultimately those used in GCMs.

References

Armijo, L. A theory for the determination of wind and precipitation velocities with Doppler radars. *Journal of the Atmospheric Sciences*, 26(3):570–573, 1969.

Askelson, M. A. and Straka, J. M. Response functions for arbitrary weight functions and data distributions. part I: Framework for interpreting the response function. *Monthly Weather Review*, 133(8):2117–2131, 2005.

Askelson, M. A., Aubagnac, J.-P., and Straka, J. M. An adaptation of the Barnes filter applied to the objective analysis of radar data. *Monthly Weather Review*, 128(9):3050–3082, 2000.

Askelson, M. A., Pauley, P. M., and Straka, J. M. Response functions for arbitrary weight functions and data distributions. part II: Response function derivation and verification. *Monthly Weather Review*, 133(8):2132–2147, 2005.

Atlas, D., Srivastava, R. C., and Sekhon, R. S. Doppler radar characteristics of precipitation at vertical incidence. *Reviews of Geophysics*, 11(1):1–35, 1973.

Barnes, S. L. A technique for maximizing details in numerical weather map analysis. *Journal of Applied Meteorology*, 3(4):396–409, 1964.

Bousquet, O. and Chong, M. A multiple-Doppler synthesis and continuity adjustment technique (MUSCAT) to recover wind components from Doppler radar measurements. *Journal of Atmospheric and Oceanic Technology*, 15(2): 343–359, 1998.

Bousquet, O., Tabary, P., and Parent du Châtelet, J. Operational multiple-Doppler wind retrieval inferred from long-range radial velocity measurements. *Journal of Applied Meteorology and Climatology*, 47(11):2929–2945, 2008.

Bringi, V. N. and Chandrasekar, V. *Polarimetric Doppler Weather Radar: Principles and Applications*. Cambridge University Press, 2001. ISBN 978-0-521-62384-1.

Byers, H. R. and Braham, R. R. Thunderstorm structure and circulation. *Journal of Meteorology*, 5(3):71–86, 1948.

Caya, A. Assimilation of radar observations into a cloud-resolving model. 2001.

Cho, Y.-H., Lee, G. W., Kim, K.-E., and Zawadzki, I. Identification and removal of ground echoes and anomalous propagation using the characteristics of radar echoes. *Journal of Atmospheric and Oceanic Technology*, 23(9):1206–1222, 2006.

Chong, M., Testud, J., and Roux, F. Three-dimensional wind field analysis from dual-Doppler radar data. part II: Minimizing the error due to temporal variation. *Journal of Climate and Applied Meteorology*, 22(7):1216–1226, 1983.

Chong, M. and Cosma, S. A formulation of the continuity equation of MUSCAT for either flat or complex terrain. *Journal of Atmospheric and Oceanic Technology*, 17(11):1556–1565, 2000.

Cifelli, R. and Rutledge, S. A. Vertical motion structure in maritime continent mesoscale convective systems: Results from a 50-MHz profiler. *Journal of the Atmospheric Sciences*, 51(18):2631–2652, 1994.

Clark, T. L., Harris, F. I., and Mohr, C. G. Errors in wind fields derived from multiple-Doppler radars: Random errors and temporal errors associated with advection and evolution. *Journal of Applied Meteorology*, 19(11):1273–1284, 1980.

Collis, S., Protat, A., and Chung, K.-S. The effect of radial velocity gridding artifacts on variationally retrieved vertical velocities. *Journal of Atmospheric and Oceanic Technology*, 27(7):1239–1246, 2010.

Collis, S., Protat, A., May, P. T., and Williams, C. Statistics of storm updraft velocities from TWP-ICE including verification with profiling measurements. *Journal of Applied Meteorology and Climatology*, 52(8):1909–1922, 2013.

Donner, L. J., Seman, C. J., Hemler, R. S., and Fan, S. A cumulus parameterization including mass fluxes, convective vertical velocities, and mesoscale effects: Thermodynamic and hydrological aspects in a general circulation model. *Journal of Climate*, 14(16):3444–3463, 2001.

Doviak, R. J. and Zrnić, D. S. *Doppler Radar and Weather Observations*. Courier Corporation, 1993. ISBN 978-0-486-45060-5.

Doviak, R. J., Ray, P. S., Strauch, R. G., and Miller, L. J. Error estimation in wind fields derived from dual-Doppler radar measurement. *Journal of Applied Meteorology*, 15(8):868–878, 1976.

Dowell, D. C. and Shapiro, A. Stability of an iterative dual-Doppler wind synthesis in Cartesian coordinates. *Journal of Atmospheric and Oceanic Technology*, 20 (11):1552–1559, 2003.

Fanyou, K. and Jietai, M. A model study of three-dimensional wind field analysis from dual-Doppler radar data. *Advances in Atmospheric Sciences*, 11(2): 162–174, 1994.

Ferrier, B. S. A double-moment multiple-phase four-class bulk ice scheme. part I: Description. *Journal of the Atmospheric Sciences*, 51(2):249–280, 1994.

Gal-Chen, T. Errors in fixed and moving frame of references: Applications for conventional and Doppler radar analysis. *Journal of the Atmospheric Sciences*, 39(10):2279–2300, 1982.

Gao, J., Xue, M., Shapiro, A., and Droegemeier, K. K. A variational method for the analysis of three-dimensional wind fields from two Doppler radars. *Monthly Weather Review*, 127(9):2128–2142, 1999.

Giangrande, S. E. and Ryzhkov, A. V. Calibration of dual-polarization radar in the presence of partial beam blockage. *Journal of Atmospheric and Oceanic Technology*, 22(8):1156–1166, 2005.

Giangrande, S. E., Luke, E. P., and Kollias, P. Automated retrievals of precipitation parameters using non-Rayleigh scattering at 95 GHz. *Journal of Atmospheric and Oceanic Technology*, 27(9):1490–1503, 2010.

Giangrande, S. E., Luke, E. P., and Kollias, P. Characterization of vertical velocity and drop size distribution parameters in widespread precipitation at ARM facilities. *Journal of Applied Meteorology and Climatology*, 51(2):380–391, 2011.

Giangrande, S. E., Collis, S., Straka, J., Protat, A., Williams, C., and Krueger, S. A summary of convective-core vertical velocity properties using ARM UHF wind profilers in oklahoma. *Journal of Applied Meteorology and Climatology*, 52(10): 2278–2295, 2013a.

Giangrande, S. E., McGraw, R., and Lei, L. An application of linear programming to polarimetric radar differential phase processing. *Journal of Atmospheric and*

Oceanic Technology, 30(8):1716–1729, 2013b.

Giangrande, S. E., Collis, S., Theisen, A. K., and Tokay, A. Precipitation estimation from the ARM distributed radar network during the MC3E campaign. *Journal of Applied Meteorology and Climatology*, 53(9):2130–2147, 2014.

Given, T. and Ray, P. S. Response of a two-dimensional dual-Doppler radar wind synthesis. *Journal of Atmospheric and Oceanic Technology*, 11(2):239–255, 1994.

Gourley, J. J., Tabary, P., and Parent du Chatelet, J. A fuzzy logic algorithm for the separation of precipitating from nonprecipitating echoes using polarimetric radar observations. *Journal of Atmospheric and Oceanic Technology*, 24(8): 1439–1451, 2007.

Heymsfield, G. M., Tian, L., Heymsfield, A. J., Li, L., and Guimond, S. Characteristics of deep tropical and subtropical convection from nadir-viewing high-altitude airborne Doppler radar. *Journal of the Atmospheric Sciences*, 67 (2):285–308, 2010.

Jakob, C. Accelerating progress in global atmospheric model development through improved parameterizations: Challenges, opportunities, and strategies. *Bulletin of the American Meteorological Society*, 91(7):869–875, 2010.

James, C. N. and Houze, R. A. A real-time four-dimensional Doppler dealiasing scheme. *Journal of Atmospheric and Oceanic Technology*, 18(10):1674–1683, 2001.

Jensen, M., Giangrande, S. E., Rutledge, S. A., and Kollias, P. The midlatitude continental convective clouds experiment (MC3E). *Bulletin of the American Meteorological Society*, (Submitted), 2015.

Jorgensen, D. P. and LeMone, M. A. Vertical velocity characteristics of oceanic convection. *Journal of the Atmospheric Sciences*, 46(5):621–640, 1989.

Kollias, P., Lhermitte, R., and Albrecht, B. A. Vertical air motion and raindrop size distributions in convective systems using a 94 GHz radar. *Geophysical Research Letters*, 26(20):3109–3112, 1999.

Kumar, V. V., Jakob, C., Protat, A., Williams, C. R., and May, P. T. Mass-flux characteristics of tropical cumulus clouds from wind profiler observations at Darwin, Australia. *Journal of the Atmospheric Sciences*, 72(5):1837–1855, 2015.

Lang, S., Tao, W.-K., Simpson, J., Cifelli, R., Rutledge, S., Olson, W., and Halverson, J. Improving simulations of convective systems from TRMM LBA: Easterly and westerly regimes. *Journal of the Atmospheric Sciences*, 64(4): 1141–1164, 2007.

Laroche, S. and Zawadzki, I. A variational analysis method for retrieval of three-dimensional wind field from single-Doppler radar data. *Journal of the Atmospheric Sciences*, 51(18):2664–2682, 1994.

Legler, D. M. and Navon, I. M. VARIATM - a FORTRAN program for objective analysis of pseudostress wind fields using large-scale conjugate-gradient minimization. *Comput. Geosci.*, 17(1):1–21, 1991.

LeMone, M. A. and Zipser, E. J. Cumulonimbus vertical velocity events in GATE. part I: Diameter, intensity and mass flux. *Journal of the Atmospheric Sciences*, 37(11):2444–2457, 1980.

Lenschow, D. H. Estimating updraft velocity from an airplane response. *Monthly Weather Review*, 104(5):618–627, 1976.

Lhermitte, R. M. and Gilet, M. Dual-Doppler radar observation and study of sea breeze convective storm development. *Journal of Applied Meteorology*, 14(7): 1346–1361, 1975.

Liou, Y.-C. and Chang, Y.-J. A variational multiple-Doppler radar three-dimensional wind synthesis method and its impacts on thermodynamic retrieval. *Monthly Weather Review*, 137(11):3992–4010, 2009.

Liou, Y.-C., Chang, S.-F., and Sun, J. An application of the immersed boundary method for recovering the three-dimensional wind fields over complex terrain using multiple-Doppler radar data. *Monthly Weather Review*, 140(5):1603–1619, 2011.

Lipps, F. B. On the anelastic approximation for deep convection. *Journal of the Atmospheric Sciences*, 47(14):1794–1798, 1990.

Lui, S., Qiu, C., Xu, Q., Zhang, P., Gao, J., and Shao, A. An improved method for Doppler wind and thermodynamic retrievals. *Advances in Atmospheric Sciences*, 22(1):90–102, 2005.

Luke, E. P. and Kollias, P. Separating cloud and drizzle radar moments during precipitation onset using Doppler spectra. *Journal of Atmospheric and Oceanic Technology*, 30(8):1656–1671, 2013.

Majcen, M., Markowski, P., Richardson, Y., Dowell, D., and Wurman, J. Multipass objective analyses of Doppler radar data. *Journal of Atmospheric and Oceanic Technology*, 25(10):1845–1858, 2008.

Matejka, T. and Bartels, D. L. The accuracy of vertical air velocities from Doppler radar data. *Monthly Weather Review*, 126(1):92–117, 1998.

Mather, J. H. and Voyles, J. W. The ARM Climate Research Facility: A review of structure and capabilities. *Bulletin of the American Meteorological Society*, 94 (3):377–392, 2012.

May, P. T. and Rajopadhyaya, D. K. Vertical velocity characteristics of deep convection over Darwin, Australia. *Monthly Weather Review*, 127(6):1056–1071, 1999.

Milbrandt, J. A. and Yau, M. K. A multimoment bulk microphysics parameterization. part II: A proposed three-moment closure and scheme description. *Journal of the Atmospheric Sciences*, 62(9):3065–3081, 2005.

Mrowiec, A. A., Rio, C., Fridlind, A. M., Ackerman, A. S., Del Genio, A. D., Pauluis, O. M., Varble, A. C., and Fan, J. Analysis of cloud-resolving simulations of a tropical mesoscale convective system observed during TWP-ICE: Vertical fluxes and draft properties in convective and stratiform regions. *Journal of Geophysical Research: Atmospheres*, 117(D19):D19201, 2012.

Navon, I. M. and Legler, D. M. Conjugate-gradient methods for large-scale minimization in meteorology. *Monthly Weather Review*, 115(8):1479–1502, 1987.

Nelson, S. P. and Brown, R. A. Error sources and accuracy of vertical velocities computed from multiple-Doppler radar measurements in deep convective storms. *Journal of Atmospheric and Oceanic Technology*, 4(1):233–238, 1987.

Ogura, Y. and Phillips, N. A. Scale analysis of deep and shallow convection in the atmosphere. *Journal of the Atmospheric Sciences*, 19(2):173–179, 1962.

Pauley, P. M. and Wu, X. The theoretical, discrete, and actual response of the Barnes objective analysis scheme for one- and two-dimensional fields. *Monthly*

Weather Review, 118(5):1145–1164, 1990.

Polak, E. and Ribiere, G. Note sur la convergence de méthodes de directions conjuguées. *ESAIM: Mathematical Modelling and Numerical Analysis - Modélisation Mathématique et Analyse Numérique*, 3(R1):35–43, 1969.

Potvin, C. K. and Wicker, L. J. Comparison between dual-Doppler and EnKF storm-scale wind analyses: Observing system simulation experiments with a supercell thunderstorm. *Monthly Weather Review*, 140(12):3972–3991, 2012.

Potvin, C. K., Betten, D., Wicker, L. J., Elmore, K. L., and Biggerstaff, M. I. 3DVAR versus traditional dual-Doppler wind retrievals of a simulated supercell thunderstorm. *Monthly Weather Review*, 140(11):3487–3494, 2012a.

Potvin, C. K., Wicker, L. J., and Shapiro, A. Assessing errors in variational dual-Doppler wind syntheses of supercell thunderstorms observed by storm-scale mobile radars. *Journal of Atmospheric and Oceanic Technology*, 29(8): 1009–1025, 2012b.

Protat, A. and Zawadzki, I. A variational method for real-time retrieval of three-dimensional wind field from multiple-Doppler bistatic radar network data. *Journal of Atmospheric and Oceanic Technology*, 16(4):432–449, 1999.

Protat, A. and Zawadzki, I. Optimization of dynamic retrievals from a multiple-Doppler radar network. *Journal of Atmospheric and Oceanic Technology*, 17(6): 753–760, 2000.

Ray, P. S., Ziegler, C. L., Bumgarner, W., and Serafin, R. J. Single- and multiple-Doppler radar observations of tornadic storms. *Monthly Weather Review*, 108 (10):1607–1625, 1980.

Rico-Ramirez, M. and Cluckie, I. Classification of ground clutter and anomalous propagation using dual-polarization weather radar. *IEEE Transactions on Geoscience and Remote Sensing*, 46(7):1892–1904, 2008.

Ryzhkov, A. V., Giangrande, S. E., Melnikov, V. M., and Schuur, T. J. Calibration issues of dual-polarization radar measurements. *Journal of Atmospheric and Oceanic Technology*, 22(8):1138–1155, 2005.

Sasaki, Y. Some basic formalisms in numerical variational analysis. *Monthly Weather Review*, 98(12):875–883, 1970.

Scialom, G. and Lemaître, Y. A new analysis for the retrieval of three-dimensional mesoscale wind fields from multiple Doppler radar. *Journal of Atmospheric and Oceanic Technology*, 7(5):640–665, 1990.

Shapiro, A. and Mewes, J. J. New formulations of dual-Doppler wind analysis. *Journal of Atmospheric and Oceanic Technology*, 16(6):782–792, 1999.

Shapiro, A., Potvin, C. K., and Gao, J. Use of a vertical vorticity equation in variational dual-Doppler wind analysis. *Journal of Atmospheric and Oceanic Technology*, 26(10):2089–2106, 2009.

Shapiro, A., Willingham, K. M., and Potvin, C. K. Spatially variable advection correction of radar data. part I: Theoretical considerations. *Journal of the Atmospheric Sciences*, 67(11):3445–3456, 2010.

Stokes, G. M. and Schwartz, S. E. The Atmospheric Radiation Measurement (ARM) program: Programmatic background and design of the cloud and radiation test bed. *Bulletin of the American Meteorological Society*, 75(7): 1201–1221, 1994.

Testud, J. and Chong, M. Three-dimensional wind field analysis from dual-Doppler radar data. part I: Filtering, interpolating and differentiating the raw data. *Journal of Climate and Applied Meteorology*, 22(7):1204–1215, 1983.

Trapp, R. J. and Doswell, C. A. Radar data objective analysis. *Journal of Atmospheric and Oceanic Technology*, 17(2):105–120, 2000.

Tridon, F., Battaglia, A., Kollias, P., Luke, E., and Williams, C. R. Signal postprocessing and reflectivity calibration of the Atmospheric Radiation Measurement program 915-MHz wind profilers. *Journal of Atmospheric and Oceanic Technology*, 30(6):1038–1054, 2013.

Williams, C. R. Vertical air motion retrieved from dual-frequency profiler observations. *Journal of Atmospheric and Oceanic Technology*, 29(10):1471–1480, 2012.

Wu, J., Del Genio, A. D., Yao, M.-S., and Wolf, A. B. WRF and GISS SCM simulations of convective updraft properties during TWP-ICE. *Journal of Geophysical Research: Atmospheres*, 114(D4):D04206, 2009.